The Early Cretaceous Shangzhuang layered mafic intrusion and its bearing on decratonization of the North China Craton

XUE-MING TENG*†, M. SANTOSH*‡ & LI TANG*§

*School of Earth Sciences and Resources, China University of Geosciences Beijing, 29 Xueyuan Road, Beijing 100083, China
‡Centre for Tectonics Resources and Exploration, Dept. of Earth Sciences, University of Adelaide, SA 5005, Australia
§Graduate School of Life and Environmental Sciences, University of Tsukuba, Ibaraki 305–8572, Japan

Abstract – The North China Craton (NCC) is one of the classic examples of decratonization through extensive lithospheric destruction during Mesozoic time. Among the various pulses of magmatism associated with cratonic erosion are the rare mafic intrusions in the Yanshan Belt. Here we investigate the Shangzhuang layered intrusion belonging to this suite, which is characterized by compositional layering with troctolite, noritic gabbro and gabbro/gabbroic anorthosite/gabbrodiorite from the bottom to top. The different lithologies of this intrusion exhibit close field relationships, similar chemical patterns and overall identical Lu–Hf isotopes indicating a co-magmatic nature. The fine-grained gabbros occurring near the margin of the intrusion display U–Pb ages similar to those of the other rocks and are considered to represent the composition of the parent magma, characterized by Fe, Mg and Ti enrichment. The magma was sourced from low-degree partial melting of spinel lherzolite sub-continental lithospheric mantle, which had been enriched by crust–mantle interaction and metasomatic fluids derived from the Mongolian oceanic slab subduction beneath the NCC during Late Palaeozoic time. In addition, limited asthenospheric or deeper-mantle materials were also locally mixed with the enriched mantle as the final source component. Our zircon U–Pb data constrain the emplacement age of this intrusion as *c.* 128–123 Ma in Early Cretaceous time, and correlates with the regional extensional tectonics between *c.* 135 and 115 Ma in the eastern and central NCC. Mantle upwelling associated with this event resulted in the thermal and chemical erosion of the lithospheric mantle, and emplacement of the parent magma of this layered intrusion.

Keywords: Shangzhuang mafic intrusion, enriched mantle, Mesozoic, lithospheric thinning, North China Craton

1. Introduction

Mafic–ultramafic magmas sourced from the mantle form in various tectonic settings and provide important clues to plate tectonic processes and crustal evolution (Polat, Appel & Fryer, 2011; Ernst & Jowitt, 2013; Jowitt & Ernst, 2013). Among these, layered sequences with podiform chromite deposits associated with ophiolites in convergent tectonic zones are considered to represent residual oceanic lithosphere and provide evidence for the subduction of oceanic lithosphere (Naldrett & von Gruenewaldt, 1989; Dilek & Furnes, 2011; Furnes, de Wit & Dilek, 2014). Another group of concentrically zoned Alaskan-type mafic–ultramafic intrusions are considered to form in arc settings and represent uplifted fragments of the deep levels of island arcs with variable contributions from the subducted slab in arc to back-arc settings (Irvine, 1974; Helmy & El Mahallawi, 2003; Batanova *et al.* 2005; Pearce & Stern, 2006; Eyuboglu *et al.* 2010; Helmy *et al.* 2014, 2015; Deng *et al.* 2015b). Layered mafic–ultramafic intrusions have been central to investigations on magma processes including differentiation, crystal cumulation and sorting, and

the formation of magmatic ore deposits (Cawthorn, 1996; Howarth & Prevec, 2013). They are commonly exposed in cratons mostly within post-collisional settings, or as small bodies within orogenic belts correlated to post-orogenic extensional settings (Su *et al.* 2012; Seo *et al.* 2013; Teng & Santosh, 2015). The mechanism of formation of Fe–Ti oxide/Cu–Ni layers/bodies in these mafic–ultramafic intrusions and related magma chamber processes are debated. The identification of the nature, petrogenesis and tectonic setting of the intrusions are critical to understand the regional geodynamics.

The thick lithospheric keels beneath Archaean crustal rocks are considered to remain stable for a long time owing to their neutral or positive buoyancy, high viscosity, mechanical strength, activation energy and linear or non-linear rheology (Shapiro, Hager & Jordan, 1999; Nyblade, 2001; King, 2005). Examples include those of the South African Craton (Boyd & Gurney, 1986) and the Western Australian Craton (Anderson, Tanimoto & Zhang, 1992). However, the North China Craton (NCC) is an exception with its eastern part having lost a significant part of the cratonic root through extensive destruction and replacement by a thinner and fertile lithospheric mantle during Mesozoic time with contemporaneous

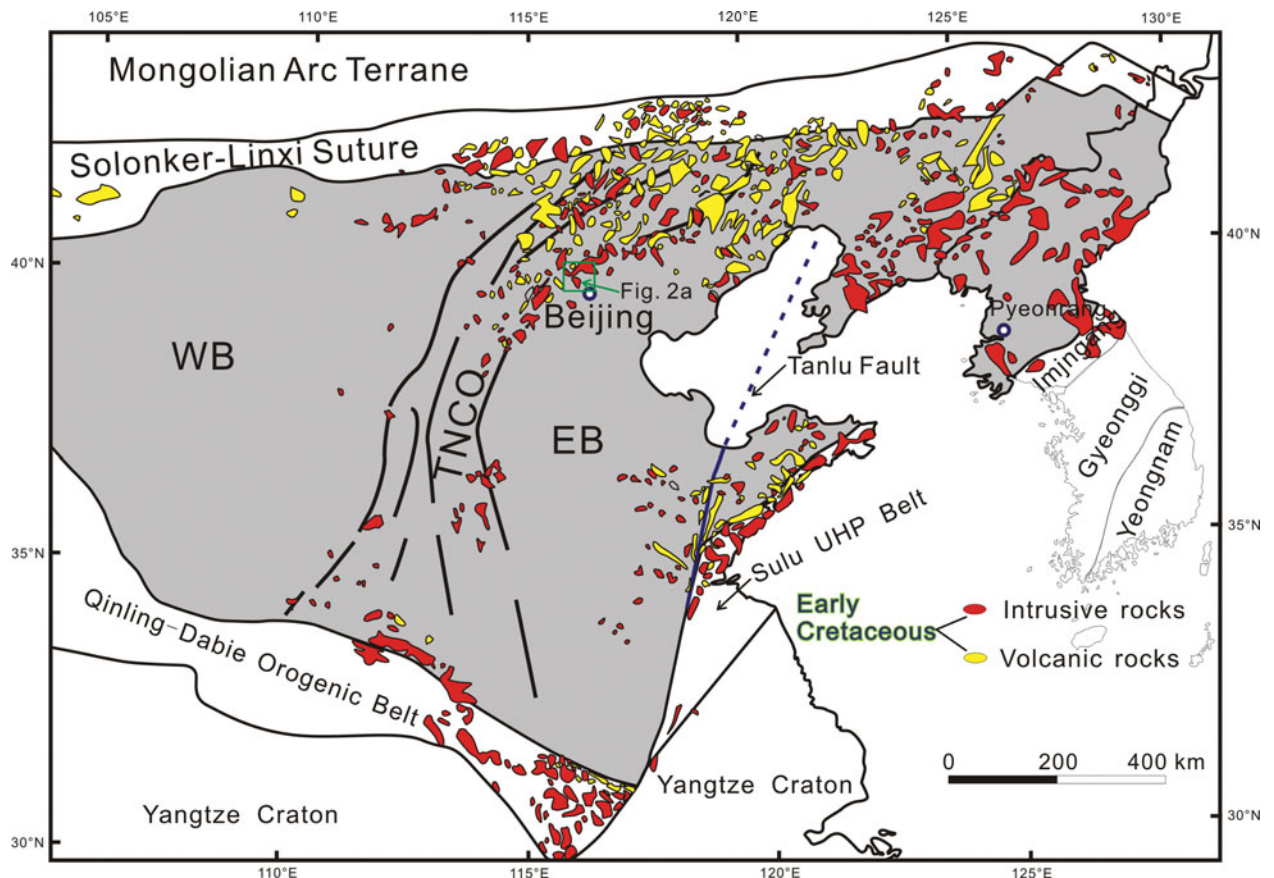†Author for correspondence: cugbtxm@126.com

Figure 1. (Colour online) Sketch geological map of the North China Craton (NCC) illustrating the East Block (EC), West Block (WB) and intervening Trans-North China Orogen (TNCO). Early Cretaceous intrusive and volcanic rocks within the NCC are also shown (modified after Zhang *et al.* 2014). The green rectangular region shows the location of the Xuejiashiliang Complex in Figure 2a.

giant magmatic events and associated metallogeny (Li *et al.* 2013, 2014*b*; Li & Santosh, 2014; Yang *et al.* 2014; Yang & Santosh, 2015). Mantle-derived ultramafic–mafic rocks provide windows to understand the mechanism of lithospheric thinning (Xu *et al.* 2004*b*; Yang *et al.* 2012). However, owing to sparse exposures of contemporaneous mantle-derived mafic rocks in the northern part of the eastern NCC (Beijing area), little is known about the nature of the lithospheric thinning in Mesozoic time in this region. The Early Cretaceous Shangzhuang Fe–Ti-oxide-bearing layered mafic intrusion exposed in the northern part of the NCC, though small in size, displays clear characteristics of layered intrusions within orogenic belts.

In this contribution, we present results from our detailed field investigations, petrography, zircon U–Pb geochronology and Lu–Hf isotopes, and geochemistry of the different rocks from this layered intrusion to evaluate the parent magma composition and crystallization process and their implications on the mantle source origin and petrogenesis. Based on the results, we further assess the geodynamic processes in the lithospheric mantle beneath the northern NCC.

2. Geological setting

The NCC is generally divided into the Eastern and Western blocks, which were amalgamated along the

300 km wide Trans-North China Orogen (TNCO) during late Palaeoproterozoic time at *c.* 1.85 Ga (Fig. 1) (Zhao *et al.* 2005; Santosh, 2010; Zhao & Zhai, 2013; Santosh *et al.* 2015, 2016), marking the final cratonization event. However, recent models illustrate the role of microcontinent amalgamation along multiple zones of ocean closure in Archaean time, which built the fundamental cratonic framework of the NCC (e.g. Zhai & Santosh, 2011; Li *et al.* 2016; Tang *et al.* 2016; Yang *et al.* 2016; Yang & Santosh, 2017). Following the Palaeoproterozoic assembly, multi-stage intraplate rifting occurred within the NCC until Neoproterozoic time, and subsequent Palaeozoic orogenesis at the margins of the craton, as represented by the Early Palaeozoic Qilian–Qinling fold belt and the Late Palaeozoic northeastern China fold belt and Mesozoic extensional tectonics accompanied by lithospheric thinning and decratonization (Zhai & Santosh, 2011 and references therein). The Mesozoic Yanshan belt is considered to be an intraplate orogenic belt, which is bounded by the Solonker–Linxi suture to the north, marking the final closure of the Mongolian ocean through continent–arc collision between the NCC and Mongolian arc terranes in Late Permian time (Davis *et al.* 2001; Xiao *et al.* 2003; Teng, Yang & Santosh, 2015).

The Early Cretaceous Xuejiashiliang Complex is located in the central part of the Yanshan intraplate orogenic belt (Wang & Zhang, 2001). It is exposed
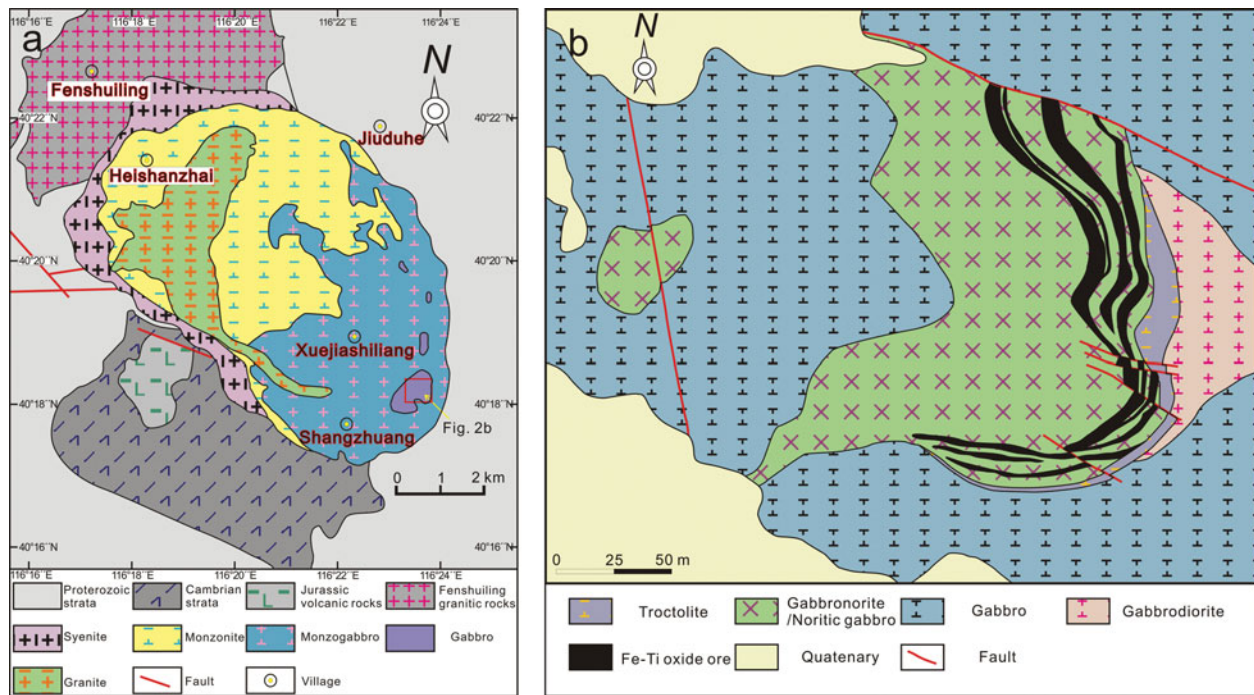
Figure 2. (Colour online) (a) Generalized geological map of Xuejiashiliang Complex (modified after Su *et al.* 2007) and (b) detailed map of Shangzhuang intrusion (modified after Liu *et al.* 2015). The red rectangular region in (a) shows the location of the Shangzhuang intrusion in (b).

over an area of ∼ 30 km^2 and shows a NW–SE strike. Five intrusive phases comprising gabbro, monzogabbro, monzonite, syenite and granite have been distinguished in this complex (Fig. 2a). The monzogabbros, located in the southeastern part of the complex, carry podiform gabbro bodies. The crescent-shaped outcrop of the syenite occurs along the northern and southwestern margins of the complex, with no direct contact relationship with the monzogabbro. The outcrop of monzonite occurs in the northwestern part of the complex and exhibits an embayed boundary against the monzogabbro. The youngest granite body intruded all the three phases except for the gabbro, which occurs within the monzogabbro (Su *et al.* 2007).

3. Characteristics of the Shangzhuang intrusion

The Shangzhuang mafic intrusion is the largest podiform intrusion among the several gabbroic bodies that were emplaced within the monzogabbro. The outcrop of the intrusion is traced over an area of ∼0.6 km^2 and strikes generally NE, and is cut by NW–SE-trending diorite dykes, and is partially overlain by Quaternary sediment (Fig. 2b). Within the intrusion, heterogeneous lithologies including troctolite, noritic gabbro/gabbronorite, gabbro and gabbrodiorite have been mapped (Liu *et al.* 2015). All the representative rock types of the intrusion are exposed in quarries, which are open cast mines for Fe–Ti oxide ores (Fig. 3a). Detailed field investigations carried out in this study led to the identification of more lithologies. Broadly, magmatic layering and cumulate textures are well preserved even at the small scale (Fig. 3b).

Troctolites in the lower part are greenish grey, and medium to coarse grained (Fig. 3c, d). Noritic gabbros are exposed at higher stratigraphic levels than the troctolite (Fig. 3e). The gabbro suite can be divided into gabbro, gabbroic anorthosite and gabbrodiorite based on field features and the relative mineral proportions. In some cases, the gabbroic anorthosites also occur as enclaves or patches within massive gabbro (Fig. 3f). The gabbros show a sharp contact with the country rocks and the marginal phase is characterized by fine-grained gabbro (Fig. 3g). Oxide ores occur as cyclic layers or lenses within the noritic gabbro and troctolite layers; some of the Fe–Ti oxide-rich domains have been highly weathered (Fig. 3h).

4. Analytical methods

4.a. Petrography

Polished thin-sections for petrography were prepared at the School of Earth and Space Sciences, Peking University. Petrographic studies were carried out at the Institute of Earths Sciences, China University of Geosciences, Beijing and mineral chemistry was analysed using an electron microprobe analyser (JEOL JXA8530F) at the Chemical Analysis Division of the Research Facility Centre for Science and Technology, University of Tsukuba, Japan.

4.b. U–Pb and Lu–Hf analyses

Zircon separation was performed at the Yu'neng Geological and Mineral Separation Survey Centre,
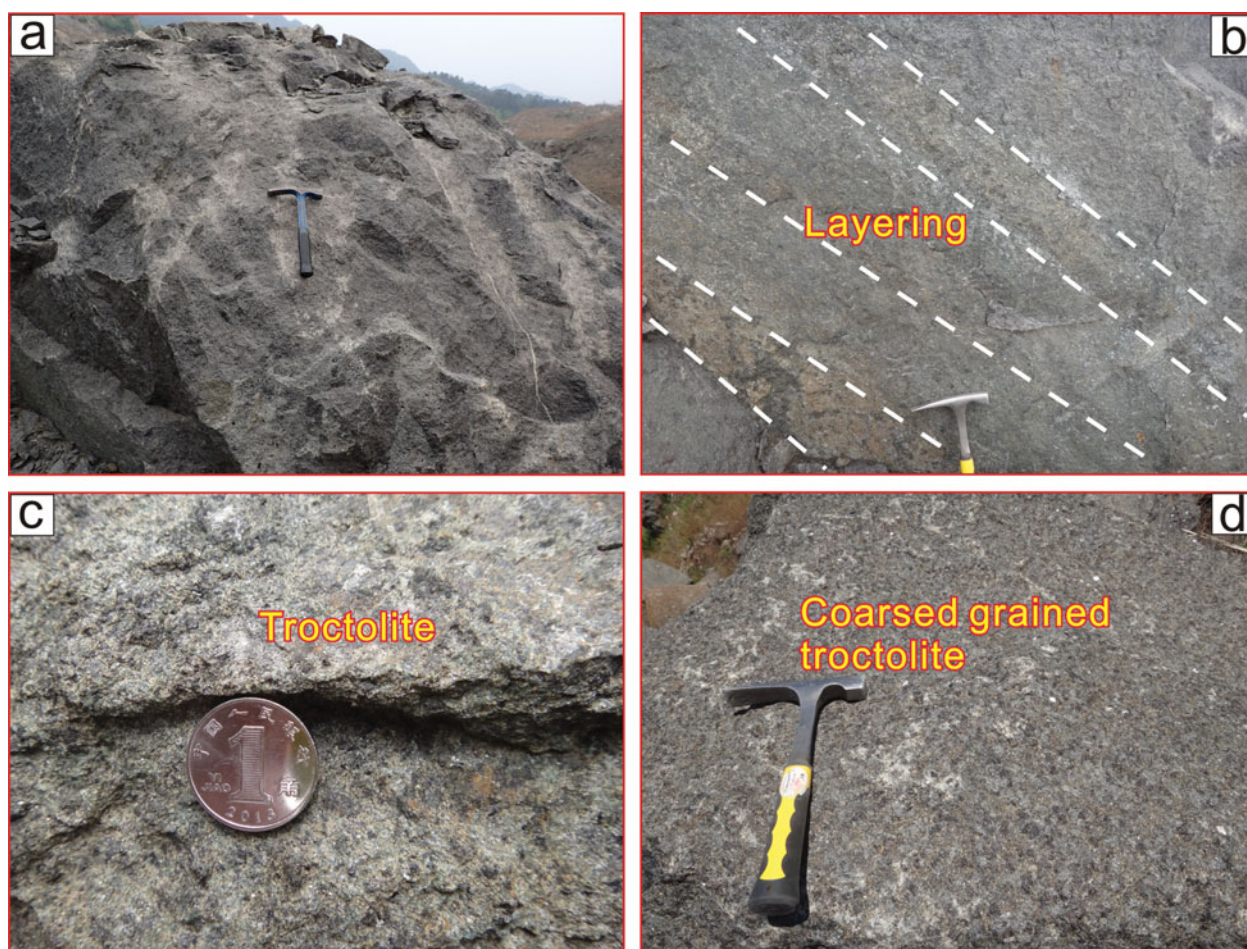
Figure 3. (Colour online) Representative field photographs of the different lithologies within the Shangzhuang mafic layered intrusion. (a) Massive nature and magmatic texture of the intrusion. (b) Silicate and oxide ore-rich interlayers. (c) Medium-grained greenish grey troctolite. (d) Coarse-grained troctolite showing megacrystic texture. Length of hammer for scale is 28 cm; diameter of coin is 1.8 cm.

Langfang City, Hebei Province, China. The zircon grains were selected by hand picking under a binocular microscope after gravimetric and magnetic separation techniques from crushed rock powder. The grains were mounted onto epoxy resin discs and then polished to expose the internal textures. Before U–Pb dating, zircon grains were imaged under transmitted, reflected light and cathodoluminescence (CL) to check the internal textures in order to choose the most suitable sites for U–Pb analysis. Zircon U–Pb dating and element analyses were carried out on a laser ablation inductively coupled plasma mass spectrometer (LA-ICP-MS) housed at the National Key Laboratory of Continental Dynamics of Northwest University, following the analytical procedures described by Yuan *et al.* (2004). In the LA-ICP-MS method, the laser spot diameter and frequency were 30 μm and 10 Hz, respectively. Zircon 91500 was employed as a standard and the standard silicate glass NIST was used to optimize the instrument. Raw data were processed using the GLITTER program to calculate isotopic ratios and ages of ^{207}Pb–^{206}Pb, ^{206}Pb–^{238}U and ^{207}Pb–^{235}U, respectively (online Supplementary Material Table S1, available at http://journals.cambridge.org/geo). Data were corrected for common lead, according to the method of Anderson (2002), and the ages were calculated by ISOPLOT 4.15 software (Yuan *et al.* 2004).

In situ zircon Hf isotopic analyses were conducted on the same spots as those where U–Pb dating was performed, or in adjacent domains with the same or similar textures, using a Neptune multicollector inductively coupled plasma mass spectrometer (MC-ICP-MS) equipped with a 193 nm Geolas Q Plus ArF exciplex laser ablation system at the Tianjin Institute of Geology and Mineral Resources, with spot sizes of 50 μm. Zircon GJ-1 was used as an external standard for *in situ* zircon Hf isotopic analyses.

4.c. Whole-rock geochemical analyses

The least altered and homogeneous portions of 15 whole-rock samples were crushed and powdered to 200 mesh for geochemical analysis after petrographic observation. Major and trace-element (including rare earth elements, REEs) analyses were conducted at the National Research Centre for Geoanalysis, Beijing. The major elements were determined by X-ray fluorescence (XRF), with analytical uncertainties ranging from 1 to 3 %. Loss on ignition was obtained using about 1 g of sample powder heated at 980 °C for

Figure 3. Continued (Colour online) (e) Medium-grained noritic gabbro. (f) Gabbroic anorthosite enclaves within massive gabbro. (g) Gabbro showing sharp contact with country rock and chilled fine-grained gabbro. (h) Highly weathered Fe–Ti oxide-rich rock. Length of hammer for scale is 28 cm; length of pen is 15 cm; diameter of coin is 1.8 cm.

30 min. The trace elements were determined as solutes by Agilent 7500ce inductively coupled plasma mass spectrometry (ICP-MS). About 50 mg of powder was dissolved for about seven days at *c*. 100 °C using HF–HNO_3 (10:1) mixtures in screw-top Teflon beakers, followed by evaporation to dryness. The material was dissolved in 7N HNO_3 and taken to incipient dryness again, and then was re-dissolved in 2 % HNO_3 to a sample/solution weight ratio of 1:1000. The analytical errors vary from 5 to 10 % depending on the concentration of any given element. An internal standard was used for monitoring drift during analyses; further details are given by Gao *et al.* (2008).

5. Results

5.a. Petrography

5.a.1. Troctolite

The troctolites are mainly composed of olivine (∼20 vol. %) and plagioclase (∼50 vol. %) with minor amounts amphibole (∼10 vol. %), phlogopite (∼7 vol. %), spinel (∼3 vol. %), magnetite and ilmenite (totally ∼5 vol. %) (Fig. 4a). The olivine and plagioclase exhibit a cumulate texture with relat-

ively euhedral to subhedral morphologies, whereas orthopyroxene, amphibole and phlogopite are present as interstitial minerals with anhedral to subhedral morphologies and occupy the space between the olivine and plagioclase crystals (Fig. 4b). Orthopyroxene forms rims around olivine grains or elongated tabular plagioclase crystals, and is considered to have resulted from reaction between olivine and residual liquids, as described by Grove & Baker (1984). Needle-shaped ilmenite exsolution lamellae are present in magnetite grains, and also occur in interstitial orthopyroxene crystals (Fig. 4c).

5.a.2. Noritic gabbro

The noritic gabbro dominantly consists of clinopyroxene (∼15 vol. %), plagioclase (∼45 vol. %), amphibole (∼20 vol. %) and orthopyroxene (∼10 vol. %), showing a gabbroic texture, together with phlogopite, magnetite and ilmenite as minor or accessory minerals (Fig. 4d, e). Amphiboles also occur as megacrysts with enclosed plagioclase, clinopyroxene, orthopyroxene and phlogopite. Orthopyroxene with ilmenite lamellae is also observed under back-scattered electron imaging (Fig. 4e).
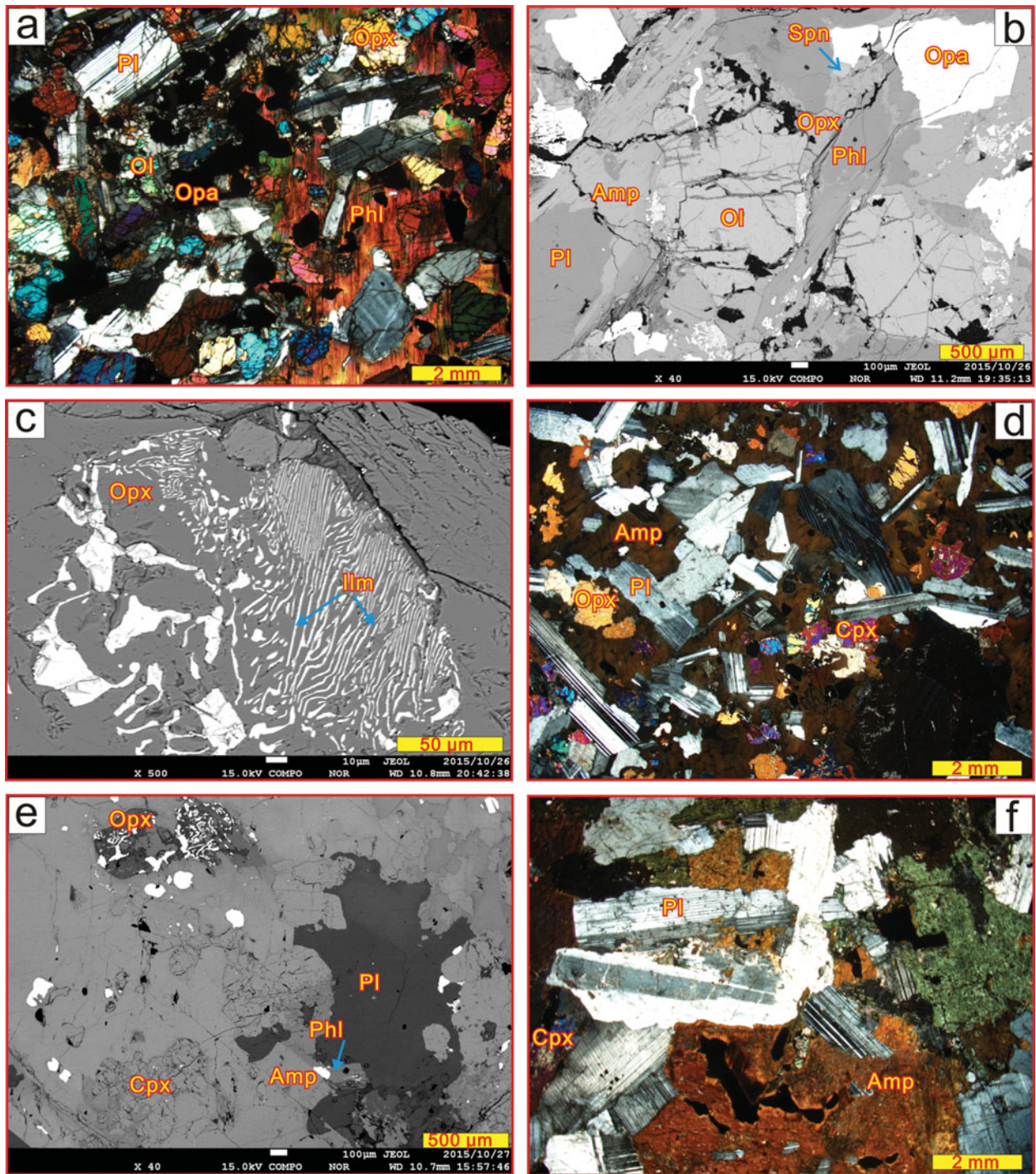
Figure 4. (Colour online) (a–f) Representative photomicrographs under crossed nicols (a, d, f, g-1063 i and kl), parallel nicols (j) and back-scattered electron image (b, c and e) showing the petrographic characteristics of the Shangzhuang rocks. (a) Major mineral assemblage of Ol + Pl + Opx + Amp + Phl in troctolite. (b) Cumulate olivine and plagioclase with interstitial amphibole and phlogopite. (c) Orthopyroxene with ilmenite lamellae. (d) Mineral assemblage of Pl + Opx + Cpx + Amp + Phl + Mgt in noritic gabbro exhibiting gabbroic texture. (e) Back-scattered electron image of rock showing ilmenite carrying orthopyroxene. (f) Gabbroic anorthosite with mega plagioclase crystals and altered amphiboles.

5.a.3. Gabbroic anorthosite

The gabbroic anorthosites are composed of plagioclase ($\sim$65 vol. %), clinopyroxene ($\sim$10 vol. %) and amphibole ($\sim$20 vol. %) with minor phlogopite and opaque minerals (including magnetite, ilmenite and spinel). The plagioclase laths are large (mostly 2 mm $\times$ 6 mm) and are randomly distributed with interstitial clinopyroxene and amphibole, phlogopite and opaque minerals (magnetite and ilmenite). The mafic minerals have been chloritized, whereas the plagioclase exhibits slight sericitization (Fig. 4f, g).
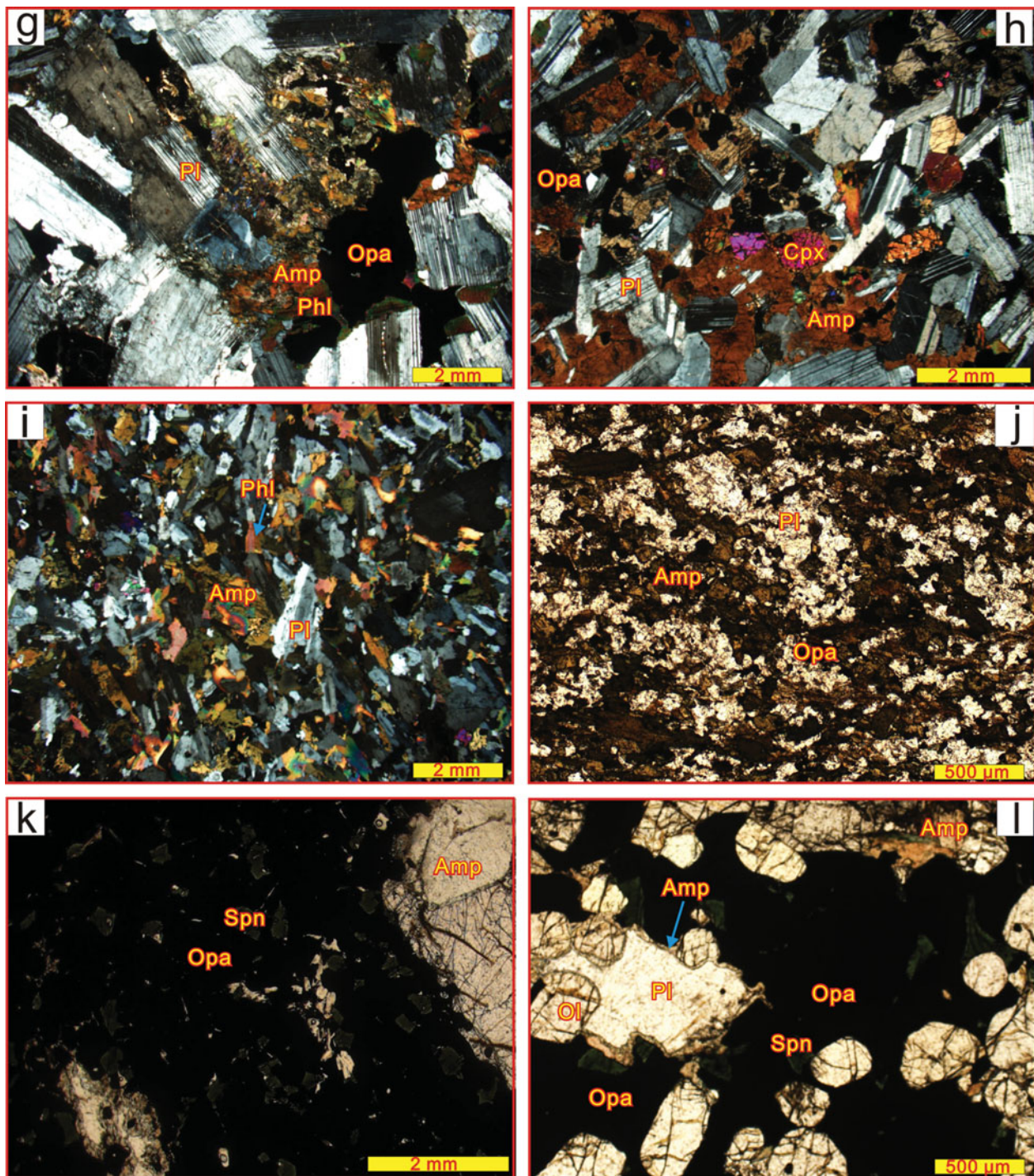
Figure 4. Continued (Colour online) (g) Gabbroic anorthosite showing mafic mineral alteration around opaque minerals. (h) Panoramic photo showing gabbroic texture for gabbro. (i) Gabbrodiorite with amphibole and plagioclase and minor phlogopite and clinopyroxene. (j) Fine-grained gabbro with amphibole, plagioclase and Fe–Ti oxides. (k) Panoramic photo showing the occurrence and texture of Fe–Ti oxide ores. (l) Olivine enclosed in plagioclase in the disseminated oxide ore and amphibole occurs as corona around the contact between plagioclase and Fe–Ti oxides. Mineral abbreviations: Pl – plagioclase; Phl – phlogopite; Opx – orthopyroxene; Cpx – clinopyroxene; Ol – olivine; Amp – amphibole; Ilm – ilmenite; Spn – spinel; Opa – opaque minerals (magnetite + ilmenite).

5.a.4. Gabbro/gabbrodiorite

The gabbro displays a typical gabbroic texture with euhedral plagioclase crystals (∼50 vol. %), clinopyroxene (∼25 vol. %) and amphibole (∼15 vol. %) as the major minerals together with opaque minerals, including magnetite and ilmenite as accessories. Clinopyroxenes are subhedral to anhedral and occur as interstitial grains between plagioclase laths. Amphiboles occur as both interstitial crystals and large anhedral crystals enclosed within clinopyroxene, plagioclase and Fe–Ti ores. Plagioclase is also observed as subhedral tabular laths randomly distributed with other minerals (Fig. 4h). When compared to gabbro, the gabbrodiorite is fine grained with dominant components of plagioclase (∼55 vol. %), amphibole

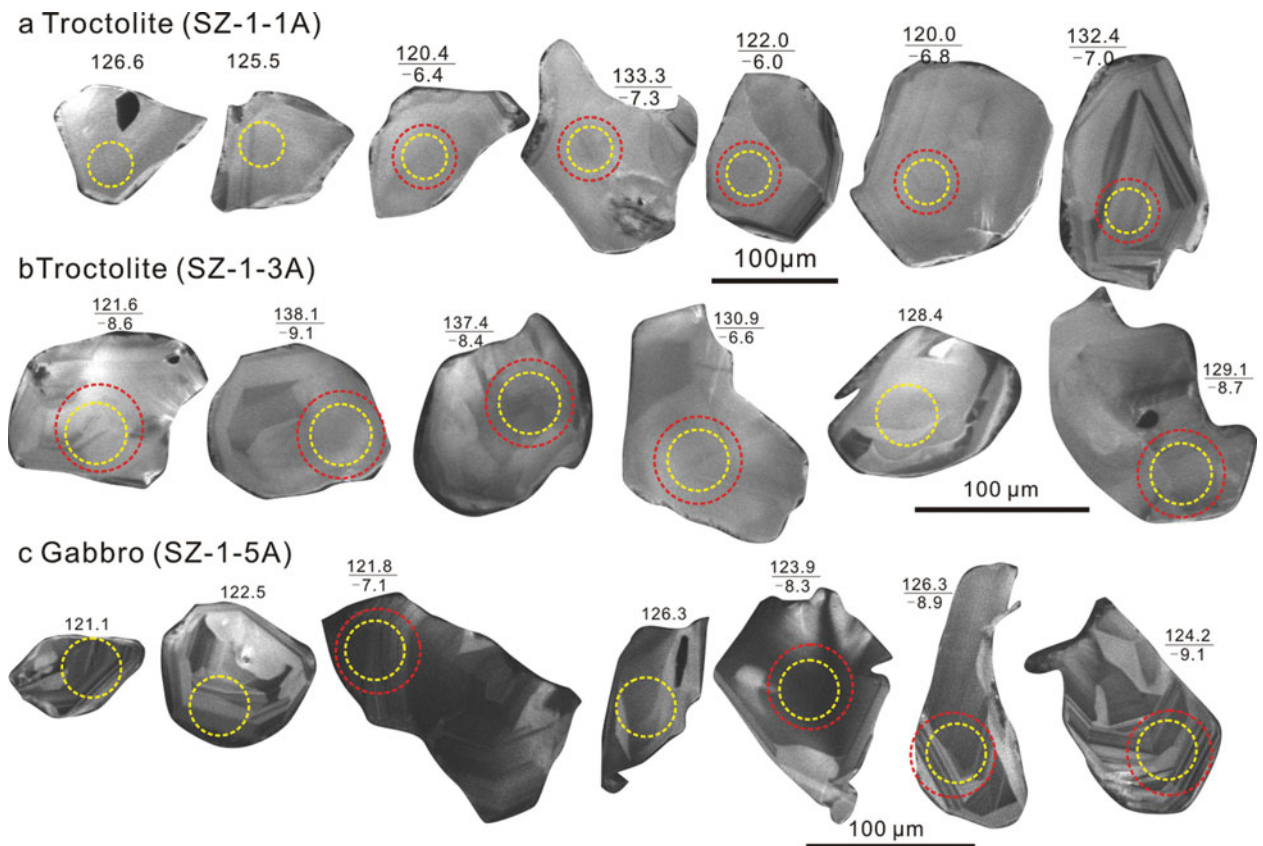Figure 5. (Colour online) Representative cathodoluminescence (CL) images of zircons from troctolites (SZ-1-1A and SZ-1-3A) and gabbro (SZ-1-5A). The analytical spots for U–Pb (small yellow dotted circles) and Lu–Hf (large red dotted circles), and age and initial $\varepsilon_{Hf}(t)$ values (in Ma) are also shown.

(~15 vol. %) and phlogopite (~15 vol. %) and subordinate clinopyroxene (~10 vol. %) and opaque minerals (Fig. 4i).

5.a.5. Fine-grained gabbro

The fine-grained gabbro is mainly composed of fine-to medium-grained amphibole and plagioclase, with interstitial opaque Fe–Ti oxides (magnetite and ilmenite). The amphiboles display dark green to light greenish grey pleochroism. The plagioclase laths are randomly distributed with a wide size range (Fig. 4j).

5.a.6. Fe–Ti oxide ores

The oxide ore is dominantly composed of magnetite and ilmenite (>60 vol. %), with spinel crystals randomly distributed within the metallic minerals (Fig. 4k). Olivine grains, plagioclase laths and phlogopite occur as isolated grains or aggregates floating within the matrix of opaque minerals. Thin rims of amphiboles are present along the boundary of the opaque mineral and plagioclase laths. Phlogopite is present as a late-stage, intercumulus mineral between the Fe–Ti oxides. The contacts between olivine/plagioclase and oxides are not sharp (Fig. 4l). The typical spinel texture can be explained as having formed by exsolution from Al-bearing opaque minerals such as magnetite or ilmenite (Ishii, Tsunogae & Santosh, 2006).

5.b. Zircon morphology and U–Pb geochronology

Six representative samples were chosen for zircon geochronology using the LA-ICP-MS method. The analytical data are listed in online Supplementary Material Table S1, available at http://journals.cambridge. org/geo, and representative CL images are shown in Figures 5 and 6. The age data are plotted in concordia diagrams in Figures 7 and 8 together with their computed weighted mean ^{206}Pb–^{238}U ages.

5.b.1. Troctolite [SZ-1-1A]

Zircon grains separated from this rock are colourless to light brown, transparent to translucent, and euhedral to subhedral prismatic and elliptical in morphology. The grains show a size range of 50–150 μm × 20–100 μm with aspect ratios of about 2.5:1 to 1:1. Most zircon grains display patchy or sector zoning, whereas a few grains exhibit a homogeneous internal texture (Fig. 5a). A total of 12 U–Pb analyses were conducted on 12 grains. Their Th contents show a range of 17.37–504.32 ppm and U contents show a range of 38.74–366.02 ppm, with Th/U ratios of 0.36–1.78 (online Supplementary Material Table S1, available at http://journals.cambridge.org/geo). On the concordia diagram (Fig. 7a), all these results fall along or near to the concordia line with high concordance (>90 %) and yield a well-defined concordia age of 125.6 ± 0.75 Ma (MSWD = 0.17, n = 12), identical to their weighted
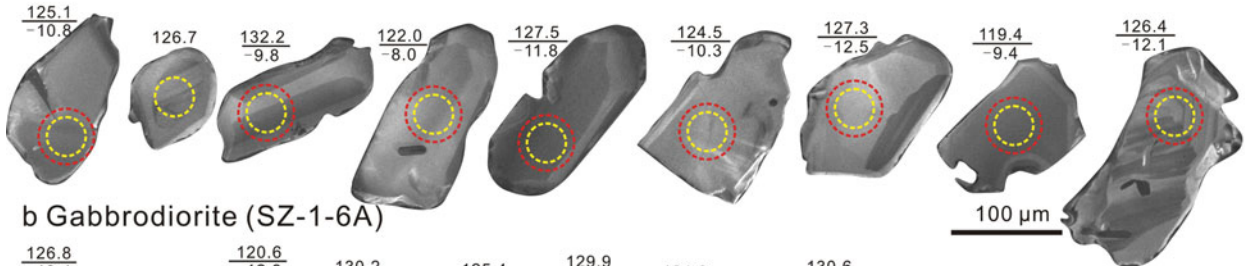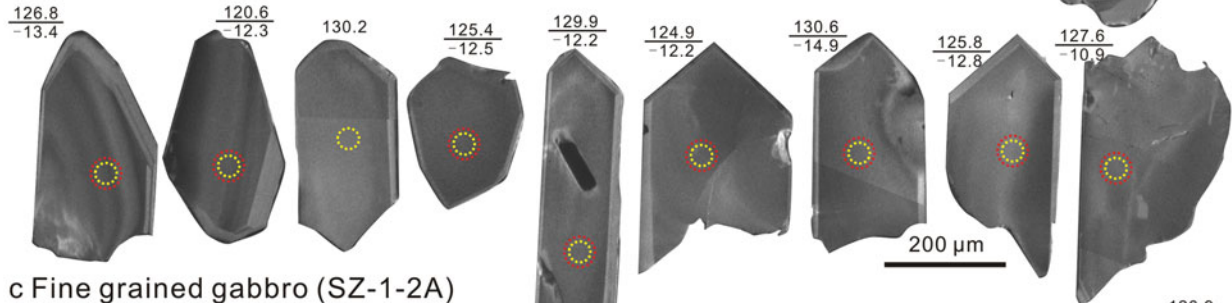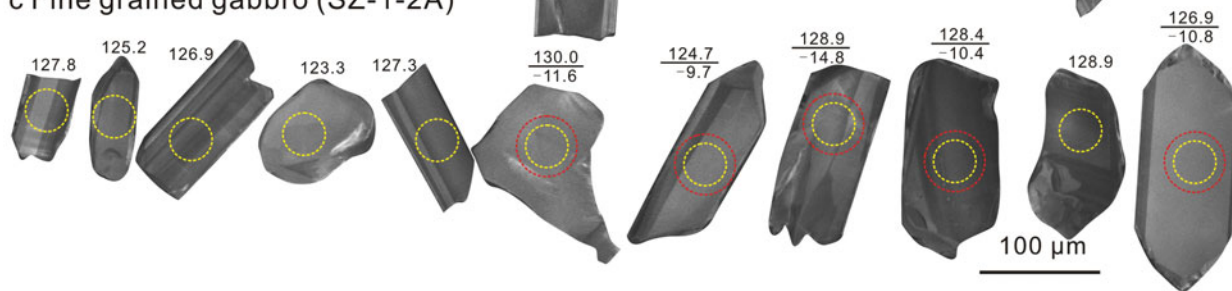
Figure 6. (Colour online) Representative cathodoluminescence (CL) images of zircons from gabbro (SZ-2-3), gabbrodiorite (SZ-1-6A) and fine-grained gabbro (SZ-1-2A). The analytical spots for U–Pb (small yellow dotted circles) and Lu–Hf (large red dotted circles), and age and initial $\varepsilon_{Hf}(t)$ values (in Ma) are also shown.
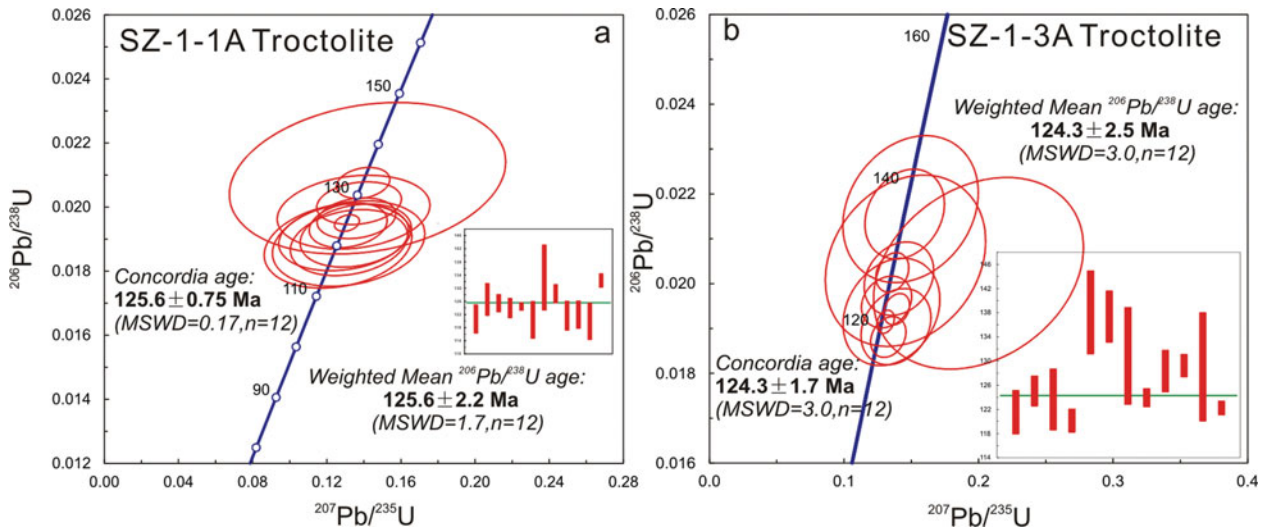
Figure 7. (Colour online) Zircon U–Pb concordia plots for sample SZ-1-1A (a) and sample SZ-1-3A (b) with inserted weighted mean ^{206}Pb–^{238}U age plot.

^{206}Pb–^{238}U age of 125.6 ± 2.2 Ma (MSWD = 1.7, n = 12). Based on the Th/U ratios and the magmatic textures, this age can be interpreted to represent the timing of crystallization of this rock.

5.b.2. Troctolite [SZ-1-3A]

The zircon grains from this sample mostly show short prismatic to stumpy morphologies, with only a few grains exhibiting an elliptical shape with rounded terminations. They are colourless to light brown, with a size range of 30–110 μm × 20–60 μm and aspect ratios ranging from 3:1 to 1:1. In CL images, the grains display a banded or patchy internal texture, with a few grains showing minor dark inherited cores and newly formed rims (Fig. 5b). A total of 15 U–Pb analyses were made on 15 grains. Except for three zircons (spots #5, #7, #12) from inherited domains
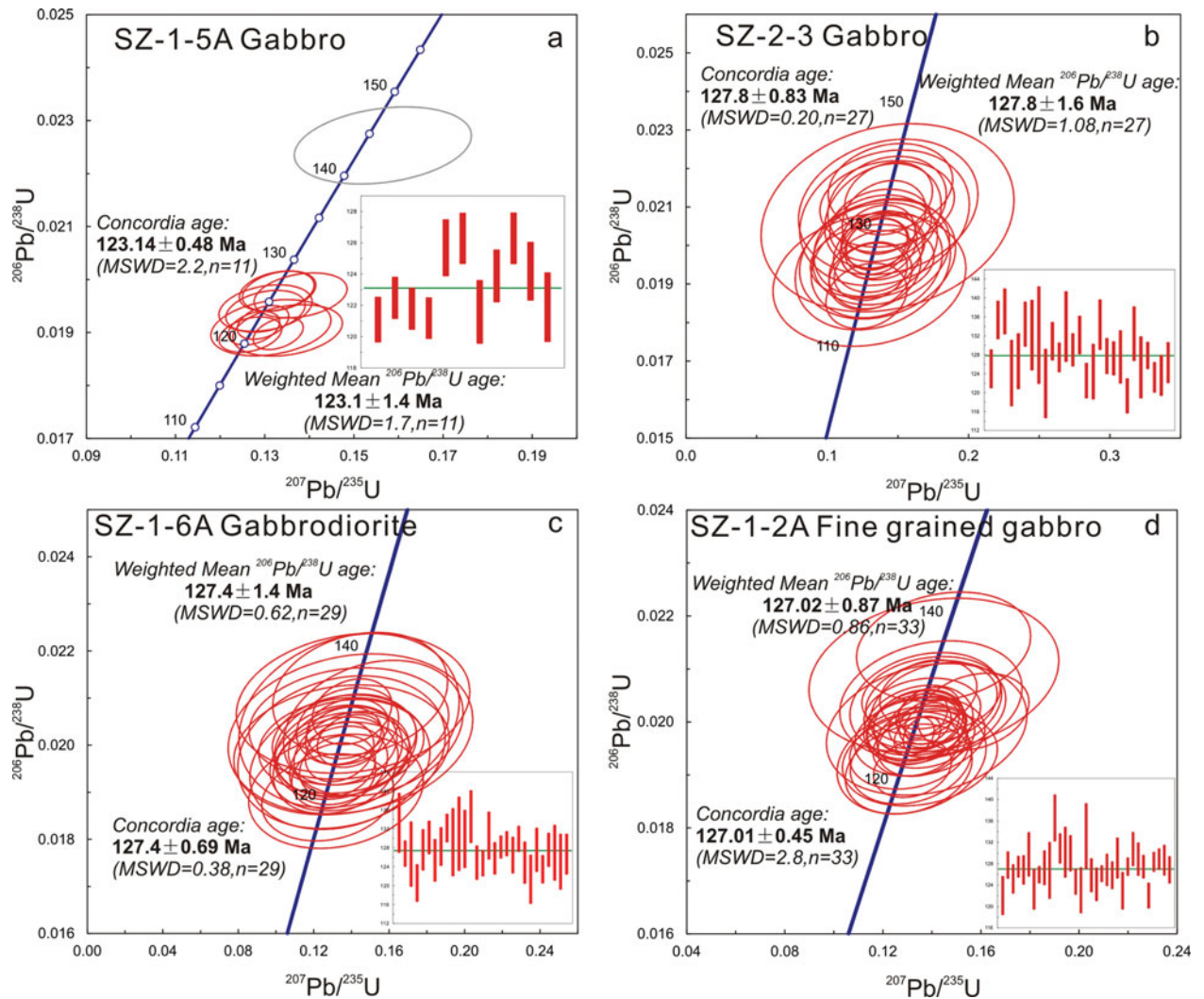
Figure 8. (Colour online) Zircon U–Pb concordia plots with inserted weighted mean ^{206}Pb–^{238}U age plot for sample SZ-1-5A (a), SZ-2-3 (b), SZ-1-6A (c) and SZ-1-2A (d).

exhibiting old ages, the other zircons exhibit Th, U and Th/U values that are in the range of 39.76–2759.09 ppm, 36.29–1074.93 ppm and 1.05–5.12, respectively (online Supplementary Material Table S1, available at http://journals.cambridge.org/geo) and are plotted along or near to the concordia line with a concordance higher than 90 %. The data yield a ^{206}Pb–^{238}U weighted mean age of 124.3 ± 2.5 Ma (MSWD of 3.0), which is almost identical to the concordia age of 124.3 ± 1.7 Ma (MSWD = 3.0, n = 12) (Fig. 7b). Both the patchy and sector zoning and Th/U values indicate a magmatic origin for these zircon grains. Thus, the age of *c.* 124.3 Ma can be interpreted as the timing of the formation of this rock.

5.b.3. Gabbro [SZ-1-5A]

Zircon grains separated from this sample are transparent to translucent, colourless to light brown, euhedral to subhedral prismatic and sub-elliptical in morphology. They vary from 20 to 150 μm in length and 15 to 80 μm in width, with aspect ratios ranging from 3.5:1 to 1.25:1. Most of them display banded or linear zoning, whereas some grains exhibit a patchy or rel-

atively homogeneous internal texture (Fig. 5c). A total of 12 spots on the magmatic domains were analysed from 12 zircon grains. Their Th contents show a range of 188–2536.91 ppm and U contents show a range of 342.93–1974.79 ppm, with Th/U ratios of 0.48–1.70 (online Supplementary Material Table S1, available at http://journals.cambridge.org/geo). On the U–Pb concordia diagram (Fig. 8a), all of the results fall along or near the concordia line with a concordance higher than 94 %. Except for one grain (spot #4) that exhibits an older inherited age (*c.* 144 Ma), the other 11 analyses yield a weighted ^{206}Pb–^{238}U mean age of 123.1 ± 1.4 Ma (MSWD = 1.7) and concordia age of 123.14 ± 0.48 Ma (MSWD = 2.2). Based on the Th/U ratios and the magmatic textures, the *c.* 123.1 Ma age can be interpreted as the timing of crystallization of this rock.

5.b.4. Gabbro [SZ-2-3]

Zircon grains from this sample are colourless to light brown, transparent to translucent, and mostly show a prismatic and ellipsoidal or sub-rounded

morphology with lengths varying from 70–200 µm and a length to width ratio of 1:1–3:1. They mostly display banded, sector or patchy zoning with a few zircons displaying a homogeneous internal texture. Some grains also possess small dark-coloured inherited domains (Fig. 6a). A total of 27 spots were analysed on 27 grains. Their Th contents range from 30.51.27–223.43 ppm and U contents range from 40.04–137.35 ppm with Th/U ratios ranging from 0.74–1.63 (online Supplementary Material Table S1, available at http://journals.cambridge.org/geo). All the 27 spots are highly concordant and distributed as a cluster along the concordia line with a well-defined concordia age of 127.8 ± 0.83 Ma (MSWD = 0.20). The data also yield an almost identical weighted ^{206}Pb–^{238}U mean age of 127.8 ± 1.6 Ma (MSWD = 1.08) (Fig. 8b). The banded, patchy or sector zoning and high Th/U values indicate a magmatic origin of these zircon grains, and the 127.8 Ma age is interpreted as the timing of formation of this rock.

5.b.5. Gabbrodiorite [SZ-1-6A]

The zircons grains from this sample are transparent to translucent and colourless, with a size of 200–500 µm × 100–250 µm and aspect ratios of 4:1 to 1.5:1. Most of these grains exhibit a long prismatic shape with sharp to rounded terminations, while a few grains occur as ellipsoidal or sub-rounded grains. Almost all of them exhibit a banded internal texture and only a few grains have a homogeneous texture (Fig. 6b). A total of 29 spots were analysed on 29 grains and the results show Th contents ranging from 22.67–318.05 ppm and U contents of 35.26–178.83 ppm with Th/U ratios in a large range of 0.60–1.78 (online Supplementary Material Table S1, available at http://journals.cambridge.org/geo). All the 29 spots form a single cluster along the concordia line with concordance higher than 95%. They defined a concordia age of 127.4 ± 0.69 Ma (MSWD = 0.38) and weighted ^{206}Pb–^{238}U mean age of 127.4 ± 1.4 Ma (MSWD = 0.62) (Fig. 8c). We interpret the age of *c.* 127.4 Ma as the timing of formation of this rock based on the magmatic features of the zircons (including high Th/U ratios and internal texture).

5.b.6. Fine-grained gabbro [SZ-1-2A]

The zircon grains in this sample mostly show a long prismatic morphology, with a few grains exhibiting an elliptical shape with round terminations. Most of the grains are colourless, and some carrying mineral inclusions show a tawny appearance. The grains vary in size from 60 to 250 µm in length and 20 to 80 µm in width, with aspect ratios ranging from 3.5:1 to 1:1. Under CL imaging, they show banded or patchy zoning, or a homogeneous internal texture (Fig. 6c). A total of 33 analyses were carried out on 33 grains. The results show Th and U contents varying from 43.32–1287.68 ppm and 58.09–459.33 ppm, respectively, and Th/U val-

ues of 0.66 to 2.80 (online Supplementary Material Table S1, available at http://journals.cambridge.org/geo). The data show a high concordance (>85%) and cluster along or very near to the concordia line yielding an age of 127.01 ± 0.45 Ma (MSWD = 2.8, n = 33). The weighted ^{206}Pb–^{238}U age is almost identical to the concordia age of 127.02 ± 0.87 Ma (MSWD = 0.86, n = 33) (Fig. 8d). We interpret the *c.* 127 Ma age as the timing of formation of this rock based on the magmatic features of the zircons (including high Th/U ratios and patchy linear zoning).

5.c. Zircon Lu–Hf isotopes

Representative zircon grains were selected for *in situ* Hf isotope analysis after zircon U–Pb analysis. A total of 54 spots were analysed on 54 grains from the six samples. The results are listed in Table 1 and illustrated in Figure 9. The data show that most of the ^{176}Lu/^{177}Hf ratios are less than 0.002, indicating the absence of any major enrichment of radiogenic Hf after the formation of the zircons. Thus, the ^{176}Hf/^{177}Hf ratios can be used as a robust reference to deduce the origin (Wu *et al.* 2007). The $f_{Lu/Hf}$ values display a tight range from −0.95 to −1.00, which are obviously lower than the $f_{Lu/Hf}$ values of mafic crust (−0.34, Amelin, Lee & Halliday, 2000) and sialic crust (−0.72, Vervoort & Patchett, 1996). Wu *et al.* (2007) suggested that the two-stage model age is more appropriate for these rocks than the single-stage model to evaluate the time of source material extraction from the depleted mantle or the residence time of the source material in the crust. The discrepancy between the two-stage model age and actual model age becomes larger when the ages of the zircons are much younger.

Six zircons from sample SZ-1-1A analysed for *in situ* Hf isotopic composition exhibit initial ^{176}Hf/^{177}Hf ratios varying from 0.282482 to 0.282526 and $\varepsilon_{Hf}(t)$ values ranging from −7.3 to −6.0 when calculated with respect to the corresponding U–Pb age. Their Hf depleted mantle model ages (T$_{DM}$) and Hf crustal model ages (T$_{DM}{}^C$) range from 1008–1067 Ma and 1565–1657 Ma, respectively. Seven analyses were carried out on selected zircon grains from sample SZ-1-3A, and the results show initial ^{176}Hf/^{177}Hf ratios in the range of 0.2822844 to 0.282505. They show variation in $\varepsilon_{Hf}(t)$ values from −14.5 to −6.6. The Hf depleted mantle model ages (T$_{DM}$) of these zircons range from 1033 Ma to 1346 Ma and the Hf crustal model ages (T$_{DM}{}^C$) from 1607–2105 Ma against their corresponding U–Pb ages.

Five spots on selected zircon grains from gabbro (sample SZ-1-5A) yielded initial ^{176}Hf/^{177}Hf values between 0.282337 and 0.282496 and negative $\varepsilon_{Hf}(t)$ values between −12.2 and −7.1 with an average of −9.1, when calculated by their own ^{206}Pb–^{238}U age. The depleted mantle ages (T$_{DM}$) and crustal residence ages (T$_{DM}{}^C$) range from 1060–1301 Ma and 1632–1974 Ma, respectively. A total of 11 Lu–Hf analyses were conducted on zircon grains from another gabbro

Table 1. LA-MC-ICP-MS Lu–Hf isotope data on zircons for SZ-1-1A (troctolite), SZ-1-3A (troctolite), SZ-1-5A (gabbro), SZ-2-3 (gabbro), SZ-1-6A (gabbrodiorite) and SZ-1-2A (fine-grained gabbro) from the Shangzhuang intrusion in this study

No.	Age (Ma)	^{176}Yb/^{177}Hf	^{176}Lu/^{177}Hf	^{176}Hf/^{177}Hf	1σ	^{176}Hf/^{177}Hf$_i$	$\varepsilon_{Hf}(0)$	$\varepsilon_{Hf}(t)$	T_{DM} (Ma)	T_{DM}^{C} (Ma)	$f_{Lu/Hf}$
SZ-1-1A-04	124.0	0.011267	0.000362	0.282508	0.000026	0.282508	−9.3	−6.6	1035	1605	−0.99
SZ-1-1A-06	120.4	0.006816	0.000250	0.282518	0.000027	0.282517	−9.0	−6.4	1020	1587	−0.99
SZ-1-1A-07	133.3	0.004968	0.000188	0.282482	0.000024	0.282482	−10.2	−7.3	1067	1657	−0.99
SZ-1-1A-10	122.0	0.008173	0.000281	0.282527	0.000025	0.282526	−8.7	−6.0	1008	1565	−0.99
SZ-1-1A-11	120.0	0.006985	0.000264	0.282506	0.000029	0.282505	−9.4	−6.8	1036	1614	−0.99
SZ-1-1A-12	132.4	0.013464	0.000512	0.282493	0.000025	0.282491	−9.9	−7.0	1061	1637	−0.98
SZ-1-2A-14	130.0	0.012215	0.000384	0.282364	0.000017	0.282363	−14.4	−11.6	1235	1926	−0.99
SZ-1-2A-15	124.7	0.021710	0.000615	0.282422	0.000022	0.282421	−12.4	−9.7	1162	1799	−0.98
SZ-1-2A-17	133.2	0.016900	0.000494	0.282334	0.000015	0.282333	−15.5	−12.6	1280	1991	−0.99
SZ-1-2A-19	124.2	0.010940	0.000351	0.282376	0.000018	0.282375	−14.0	−11.3	1217	1902	−0.99
SZ-1-2A-22	125.9	0.033405	0.000831	0.282276	0.000027	0.282274	−17.5	−14.9	1373	2127	−0.97
SZ-1-2A-26	130.8	0.026923	0.000707	0.282372	0.000024	0.282370	−14.2	−11.4	1235	1910	−0.98
SZ-1-2A-27	128.9	0.019147	0.000442	0.282276	0.000033	0.282275	−17.5	−14.8	1359	2124	−0.99
SZ-1-2A-28	127.5	0.049944	0.001195	0.282404	0.000031	0.282401	−13.0	−10.3	1206	1842	−0.96
SZ-1-2A-30	128.4	0.041059	0.000857	0.282402	0.000035	0.282399	−13.1	−10.4	1198	1845	−0.97
SZ-1-2A-32	128.7	0.030114	0.000705	0.282363	0.000039	0.282361	−14.5	−11.7	1247	1930	−0.98
SZ-1-2A-33	126.9	0.030414	0.000703	0.282391	0.000039	0.282389	−13.5	−10.8	1208	1869	−0.98
SZ-1-3A-01	121.6	0.005278	0.000164	0.282454	0.000024	0.282454	−11.2	−8.6	1105	1728	−1.00
SZ-1-3A-02	125.1	0.011835	0.000458	0.282285	0.000040	0.282284	−17.2	−14.5	1346	2105	−0.99
SZ-1-3A-06	138.1	0.004049	0.000117	0.282430	0.000029	0.282430	−12.1	−9.1	1136	1771	−1.00
SZ-1-3A-08	137.4	0.007015	0.000187	0.282450	0.000031	0.282449	−11.4	−8.4	1111	1728	−0.99
SZ-1-3A-09	130.9	0.003341	0.000091	0.282505	0.000024	0.282505	−9.4	−6.6	1033	1607	−1.00
SZ-1-3A-11	128.4	0.018133	0.000523	0.282391	0.000022	0.282390	−13.5	−10.7	1203	1867	−0.98
SZ-1-3A-14	129.1	0.011625	0.000328	0.282446	0.000032	0.282446	−11.5	−8.7	1120	1741	−0.99
SZ-1-5A-03	121.8	0.030521	0.000746	0.282498	0.000021	0.282496	−9.7	−7.1	1060	1632	−0.98
SZ-1-5A-04	143.7	0.034660	0.001388	0.282341	0.000020	0.282337	−15.2	−12.2	1301	1974	−0.96
SZ-1-5A-09	123.9	0.018842	0.000596	0.282462	0.000029	0.282460	−11.0	−8.3	1106	1711	−0.98
SZ-1-5A-10	126.3	0.035429	0.000909	0.282444	0.000024	0.282442	−11.6	−8.9	1140	1751	−0.97
SZ-1-5A-11	124.2	0.011795	0.000410	0.282438	0.000027	0.282437	−11.8	−9.1	1134	1764	−0.99
SZ-1-6A-01	133.3	0.012878	0.000371	0.282359	0.000022	0.282358	−14.6	−11.7	1242	1935	−0.99
SZ-1-6A-02	126.8	0.041532	0.002192	0.282317	0.000030	0.282312	−16.1	−13.5	1364	2042	−0.93
SZ-1-6A-03	126.7	0.013246	0.000414	0.282277	0.000020	0.282276	−17.5	−14.8	1356	2123	−0.99
SZ-1-6A-04	120.6	0.022946	0.000673	0.282351	0.000021	0.282350	−14.9	−12.3	1262	1961	−0.98
SZ-1-6A-07	125.4	0.032905	0.000974	0.282343	0.000022	0.282341	−15.2	−12.5	1283	1977	−0.97
SZ-1-6A-08	128.3	0.012180	0.000370	0.282313	0.000020	0.282312	−16.2	−13.5	1305	2041	−0.99
SZ-1-6A-10	129.2	0.016387	0.000462	0.282412	0.000025	0.282411	−12.7	−9.9	1171	1818	−0.99
SZ-1-6A-12	129.9	0.037497	0.000884	0.282349	0.000022	0.282346	−15.0	−12.2	1273	1963	−0.97
SZ-1-6A-13	134.6	0.015252	0.000410	0.282298	0.000021	0.282297	−16.8	−13.9	1327	2071	−0.99
SZ-1-6A-14	124.9	0.032873	0.000851	0.282353	0.000028	0.282351	−14.8	−12.2	1266	1956	−0.97
SZ-1-6A-16	130.6	0.030752	0.000889	0.282271	0.000019	0.282268	−17.7	−14.9	1382	2137	−0.97
SZ-1-6A-17	125.8	0.024041	0.000738	0.282334	0.000022	0.282332	−15.5	−12.8	1289	1997	−0.98
SZ-1-6A-21	129.9	0.040230	0.001116	0.282361	0.000026	0.282358	−14.6	−11.8	1264	1937	−0.97
SZ-1-6A-26	127.6	0.042757	0.001040	0.282389	0.000030	0.282386	−13.6	−10.9	1222	1875	−0.97
SZ-2-3-01	125.1	0.017069	0.000463	0.282390	0.000023	0.282389	−13.5	−10.8	1202	1870	−0.99
SZ-2-3-08	132.2	0.016681	0.000496	0.282415	0.000019	0.282413	−12.6	−9.8	1169	1811	−0.99
SZ-2-3-09	122.0	0.017854	0.000516	0.282472	0.000021	0.282471	−10.6	−8.0	1090	1689	−0.98
SZ-2-3-11	127.5	0.014330	0.000381	0.282361	0.000030	0.282360	−14.5	−11.8	1239	1933	−0.99
SZ-2-3-16	124.5	0.024329	0.000516	0.282406	0.000027	0.282405	−12.9	−10.3	1181	1835	−0.98
SZ-2-3-19	127.3	0.018467	0.000442	0.282341	0.000024	0.282340	−15.2	−12.5	1269	1979	−0.99
SZ-2-3-21	119.4	0.019795	0.000506	0.282432	0.000023	0.282431	−12.0	−9.4	1145	1780	−0.98
SZ-2-3-22	132.5	0.035777	0.000899	0.282282	0.000021	0.282280	−17.3	−14.5	1367	2110	−0.97
SZ-2-3-23	125.4	0.028572	0.000749	0.282290	0.000019	0.282288	−17.1	−14.4	1351	2097	−0.98
SZ-2-3-24	127.9	0.020113	0.000596	0.282381	0.000021	0.282380	−13.8	−11.1	1219	1890	−0.98
SZ-2-3-27	126.4	0.021832	0.000606	0.282353	0.000021	0.282351	−14.8	−12.1	1258	1954	−0.98

Note: ^{176}Lu decay constant $\lambda = 1.867 \times 10^{-11}$ yr^{-1} (Söderlund *et al.* 2004); chondritic values: (^{176}Lu/^{177}Hf)$_{CHUR}$ = 0.0332 ± 0.0002, (^{176}Hf/^{177}Hf)$_{CHUR}$ = 0.282772 ± 0.000029 (Blichert-Toft & Albarède, 1997); depleted mantle values: (^{176}Lu/^{177}Hf)$_{DM}$ = 0.0384, (^{176}Hf/^{177}Hf)$_{DM}$ = 0.28325 (Griffin *et al.* 2000); Hf$_i$: initial Hf isotope composition for U–Pb age; f$_{Lu/Hf}$ = (^{176}Lu/^{177}Hf)$_{sample}$/(^{176}Lu/^{177}Hf)$_{CHUR}$−1; T_{DM} = 1/λ × ln(1 + ((^{176}Hf/^{177}Hf)$_{sample}$ − (^{176}Hf/^{177}Hf)$_{DM}$)/((^{176}Lu/^{177}Hf)$_{sample}$ − (^{176}Lu/^{177}Hf)$_{DM}$)); T_{DM} ^{C} = 1/λ × ln(1 + ((^{176}Hf/^{177}Hf)$_{sample,t}$ − (^{176}Hf/^{177}Hf)$_{DM,t}$)/((^{176}Lu/^{177}Hf)$_c$ − (^{176}Lu/^{177}Hf)$_{DM}$)) + t; (^{176}Lu/^{177}Hf)$_c$ = 0.015; t = crystallization time of zircon. The ^{176}Hf/^{177}Hf ratios reported were corrected according to the recommended value of the standard zircon 91500.

(SZ-2-3). The results exhibit initial ^{176}Hf/^{177}Hf values ranging from 0.282280 to 0.282471, and negative $\varepsilon_{Hf}(t)$ values between −14.5 and −8.0 with an average of −11.3, when calculated by their ^{206}Pb–^{238}U age. Their depleted mantle ages (T_{DM}) and crustal residence ages (T_{DM}^{C}) are in the range of 1090 to 1367 Ma and 1689 to 2110 Ma, respectively.

Fourteen spots were analysed on representative zircon grains from sample SZ-1-6A (gabbrodiorite). They show initial ^{176}Hf/^{177}Hf values ranging from 0.282268 to 0.282411, and negative $\varepsilon_{Hf}(t)$ values between −14.9 and −9.9 with an average of −13.0, when calculated by their ^{206}Pb–^{238}U age. Their depleted mantle ages and crustal residence ages (T_{DM}^{C})
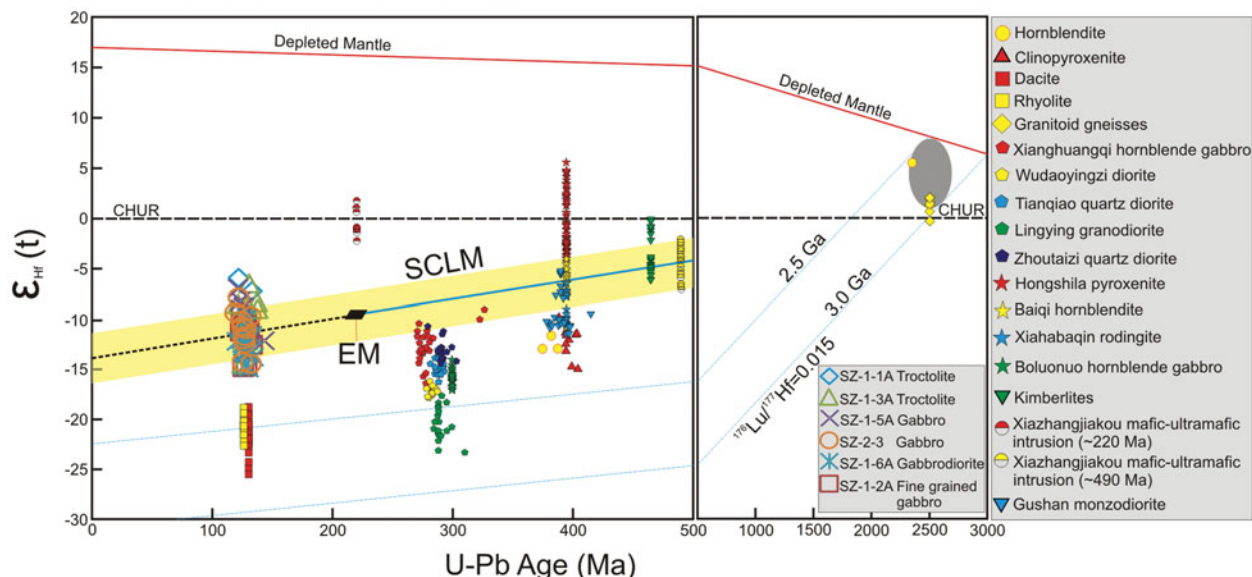
Figure 9. (Colour online) Plot of ε$_{Hf}$(t) v. U–Pb age for the Shangzhuang samples and data from Early Ordovician to Early Cretaceous magmatic bodies in northern Hebei and kimberlites in the eastern North China Craton. Hf isotopic compositions of zircons from hornblendite and clinopyroxenite are from Teng, Yang & Santosh (2015). Hf isotopic compositions of zircons from dacite and rhyolite are from Yang *et al.* (2006b). Hf isotopic compositions of zircons from Neoarchaean granitoid gneisses are from Liu *et al.* (2011). Hf isotopic compositions of zircons from Xianghuangqi hornblende gabbro, Wudaoyingzi diorite, Tianqiao quartz diorite, Lingying granodiorite and Zhoutaizi quartz diorite are from Zhang *et al.* (2009a). Hf isotopic compositions of zircons from Hongshila pyroxenite, Xiahabaqin rodingite, Baiqi hornblendite and Boluonuo hornblende gabbro are from Zhang *et al.* (2009b). Hf isotopic compositions of zircons from kimberlites in the eastern North China Craton are from Zhang & Yang (2007). Hf isotopic compositions of zircons from Xiaozhangjiakou mafic–ultramafic complex are from Tian *et al.* (2007). Hf isotopic compositions of zircons from Gushan monzodiorite are from Zhang *et al.* (2007). The Hf isotopic value of enriched mantle of the North China Craton is from Chen *et al.* (2008) and Yang *et al.* (2006a).

are in the range of 1171 to 1382 Ma and 1818 to 2137 Ma, respectively.

Eleven analyses on fine-grained gabbro (sample SZ-1-2A) display initial ^{176}Hf/^{177}Hf ratios varying from 0.282274 to 0.282421 and ε$_{Hf}$(t) values ranging from −14.9 to −9.7 calculated with respect to the corresponding U–Pb age. The ε$_{Hf}$ single-stage model ages (T$_{DM}$) range from *c.* 1162 Ma to *c.* 1373 Ma, and two-stage model ages (T$_{DM}$^{C}) from *c.* 1799 Ma to 2127 Ma.

In the ε$_{Hf}$(t) versus U–Pb age plot (Fig. 9), data are plotted on or near the array of the presumed sub-continental lithospheric mantle (SCLM) area (yellow shaded region in Fig. 9). The array and average line for the evolution of enriched SCLM are based on the following lines of argument. (1) The ε$_{Hf}$(t) value of −9.0 was estimated for enriched mantle of the NCC by Chen *et al.* (2008) and Yang *et al.* (2006a) at *c.* 220 Ma. (2) The ε$_{Hf}$(t) values for the captured ~490 Ma zircons represent an enriched mantle source which had been metasomatized by fluid or/and melt released through subduction of the Mongolian oceanic slab during Late Palaeozoic time (Tian *et al.* 2007). The average line was defined by the value of ∼−9.0 at 220 Ma and average value of ε$_{Hf}$(t) values for the captured ~490 Ma zircons, whereas the array is bounded by the maximum and minimum values of the captured zircons and the boundaries are assumed to be parallel to the average evolution line. If no more enrichment occurred after 220 Ma, the evolutionary array would follow the pat-

tern as indicated by the black broken line. If the original enriched mantle is further enriched, the evolution line and array for SCLM would exhibit more negative ε$_{Hf}$(t) values. As shown in Figure 9, the data from our zircon grains plot in the array of the presumed SCLM. We, therefore, conclude that the source of the magma is likely linked to the enriched SCLM which had been fertilized by the metasomatism induced by the subduction of the Mongolian oceanic slab during Late Palaeozoic time.

5.d. Whole-rock geochemistry

Whole-rock geochemistry data, including major, minor, trace and rare earth elements for the different rocks from the Shangzhuang intrusion are presented in Table 2. A total of 15 samples were analysed including four troctolites, two noritic gabbros, two gabbroic anorthosites, four gabbros, one gabbrodiorite and two fine-grained gabbros.

5.d.1. Alteration assessment

Though the least altered and homogeneous portions of rocks from the Shangzhuang intrusion were selected for whole-rock geochemical analysis, it is still necessary to assess the effects and extent of post-magmatic alteration on geochemical compositions before utilizing the geochemical data for

Table 2. Major, trace and rare earth concentrations of the whole-rock samples from Shangzhuang layered intrusion

Sample number	SZ-1/1A	SZ-1/1B	SZ-1/3A	SZ-1/3C	SZ-1/2A	SZ-1/2B	SZ-1/3D	SZ-3/1	SZ-1/4A	SZ-1/4B	SZ-1/5A	SZ-1/5B	SZ-2/1	SZ-2/3	SZ-1/6A
Rock type	Troc	Troc	Troc	Troc	Fgg	Fgg	Ganor	Ganor	Norg	Norg	Gabbro	Gabbro	Gabbro	Gabbro	Gabdo
Major elements (wt %)															
SiO_2	34.17	30.99	41.78	44.00	47.91	49.27	44.62	46.00	42.82	45.87	44.00	43.42	46.95	47.37	58.28
TiO_2	4.11	5.04	1.62	2.13	2.42	2.32	2.02	2.51	1.86	1.35	2.66	2.19	2.21	2.27	1.12
Al_2O_3	12.21	12.12	7.70	14.33	15.32	15.30	16.50	16.76	8.76	13.58	10.77	16.73	15.57	15.50	17.91
TFe_2O_3	28.60	32.40	15.66	15.63	12.66	11.65	13.62	11.94	14.27	12.81	16.12	16.50	12.04	12.85	5.72
MnO	0.18	0.18	0.17	0.14	0.13	0.13	0.10	0.15	0.16	0.14	0.15	0.12	0.13	0.17	0.06
MgO	12.43	11.65	19.5	9.87	4.96	4.36	6.51	4.82	16.97	11.06	9.96	8.08	5.75	5.24	2.01
CaO	4.39	3.86	8.09	9.32	7.06	6.36	10.95	8.87	10.03	10.38	12.49	7.97	7.57	7.54	3.70
K_2O	0.49	0.44	0.79	0.60	1.38	2.94	0.53	1.33	0.73	0.59	0.55	0.58	2.38	2.27	3.90
Na_2O	1.97	1.89	1.69	2.54	4.74	4.73	2.70	4.46	1.67	2.28	1.99	2.97	4.42	4.14	5.45
P_2O_5	0.18	0.16	0.65	0.20	1.30	1.24	0.12	1.37	0.76	0.27	0.16	0.14	1.39	1.15	0.42
LOI	0.28	0.09	1.26	0.21	0.73	0.46	1.71	0.49	1.03	0.40	0.18	0.18	0.73	0.35	0.40
Total	99.01	98.82	98.91	98.97	98.61	98.76	99.38	98.70	99.06	98.73	99.03	98.88	99.14	98.85	98.97
Trace elements (ppm)															
Sc	7.1	5.39	27.4	19.9	11.8	11.7	24.3	17.4	35.9	28.4	36.5	11.2	16.3	17.2	5.14
V	694	848	211	355	209	208	347	159	235	210	429	370	217	234	77.6
Cr	13.6	18.4	1340	16.2	72.7	57.9	104	23.4	1123	395	23.0	15.9	107	42.8	9.26
Co	132	120	91.2	73.0	35.6	31.8	52.9	22.8	77.4	63.9	63.3	70.3	32.5	30.5	11.9
Ni	184	171	527	87.8	45.0	38.8	48.2	12.5	441	196	71.5	75.8	73.2	41.8	10.8
Cu	78.9	84.6	47.0	19.4	47.0	39.6	41.3	14.5	60.6	101	18.1	14.6	43.6	28.3	24.7
Zn	283	295	150	129	134	141	109	153	131	101	131	255	157	145	69.9
Ga	24.3	25.6	12.7	19.0	22.3	21.8	19.5	22.5	13.5	16.2	18.5	21.2	22.9	24.0	20.4
Rb	5.18	4.22	10.6	6.48	21.1	78.6	4.99	13.7	8.28	5.40	6.31	5.48	29.7	42.9	43.6
Sr	1233	1097	701	1492	1620	1117	1470	1909	870	1159	897	1879	1976	1587	1210
Y	3.45	2.48	12.1	7.45	17.8	17.2	7.25	33.1	14.0	11.3	12.0	4.71	21.4	25.0	11.7
Zr	41.8	37.7	90.5	67.2	232	260	40.3	108	92.1	71.7	80.4	50.1	262	181	277
Nb	4.73	4.08	10.2	4.54	28.9	28.6	2.49	23.6	10.8	5.96	4.75	3.79	25.1	19.1	19.7
Ba	400	329	483	447	1291	1058	456	1362	561	452	478	559	2074	2045	2679
Hf	1.00	0.90	2.33	1.78	5.33	5.85	1.26	3.31	2.55	2.02	2.45	1.25	7.07	4.50	6.71
Ta	0.34	0.30	0.60	0.30	1.76	1.84	0.17	1.18	0.66	0.36	0.32	0.25	1.24	0.90	1.15
Pb	1.83	1.57	2.85	2.27	6.39	10.9	2.57	5.35	2.36	2.20	1.86	2.56	7.27	6.89	16.3
Th	0.45	0.33	1.20	0.57	2.73	3.41	0.27	1.43	0.94	0.53	0.49	0.50	2.21	1.33	3.07
U	0.10	0.08	0.30	0.13	0.67	0.83	0.06	0.40	0.29	0.13	0.13	0.12	0.37	0.32	0.87
La	8.83	7.49	23.1	12.4	61.5	62.8	8.62	67.9	23.8	14.4	12.8	10.6	97.2	81.1	47.9
Ce	17.5	14.9	53.5	26.7	130	131	19.3	152	57.9	33.6	30.6	20.6	196	175	86.6
Pr	2.20	1.84	7.38	3.46	16.6	16.3	2.71	20.0	7.94	4.55	4.39	2.58	24.1	21.6	10.8
Nd	8.84	6.71	31.6	14.7	65.4	67.1	12.6	89.4	34.0	20.4	20.2	11.0	94.1	84.0	38.4
Sm	1.66	1.28	6.14	3.06	11.2	10.6	2.91	15.1	6.86	4.17	4.77	2.40	15.4	14.5	8.11
Eu	0.66	0.54	2.00	1.17	3.51	3.35	1.16	4.95	2.12	1.46	1.56	1.04	4.24	4.75	2.52
Gd	1.10	0.89	4.65	2.41	7.95	6.95	2.19	12.2	5.28	3.37	3.88	1.53	9.38	10.4	3.99
Tb	0.15	0.10	0.60	0.34	0.95	0.92	0.35	1.49	0.69	0.47	0.54	0.21	1.20	1.23	0.54

Table 2. Continued

Sample number Rock type	SZ-1/1A Troc	SZ-1/1B Troc	SZ-1/3A Troc	SZ-1/3C Troc	SZ-1/2A Fgg	SZ-1/2B Fgg	SZ-1/3D Ganor	SZ-3/1 Ganor	SZ-1/4A Norg	SZ-1/4B Norg	SZ-1/5A Gabbro	SZ-1/5B Gabbro	SZ-2/1 Gabbro	SZ-2/3 Gabbro	SZ-1/6A Gabdo
Dy	0.79	0.54	2.85	1.74	4.21	4.19	1.79	7.81	3.28	2.32	2.87	1.10	5.55	6.11	2.53
Ho	0.14	0.10	0.46	0.30	0.67	0.65	0.32	1.31	0.55	0.44	0.50	0.18	0.90	1.00	0.45
Er	0.31	0.26	1.13	0.76	1.57	1.57	0.77	3.33	1.36	1.11	1.19	0.45	2.13	2.53	1.17
Tm	< 0.05	< 0.05	0.15	0.10	0.20	0.21	0.11	0.43	0.17	0.16	0.17	0.07	0.27	0.34	0.17
Yb	0.29	0.22	0.92	0.65	1.21	1.18	0.59	2.57	1.01	0.89	1.05	0.40	1.67	2.02	1.09
Lu	< 0.05	< 0.05	0.13	0.10	0.15	0.15	0.09	0.35	0.14	0.13	0.13	0.05	0.23	0.27	0.16
Th/Ta	1.32	1.10	2.00	1.90	1.55	1.85	1.59	1.21	1.42	1.47	1.53	2.00	1.78	1.48	2.67
Ba/Zr	9.57	8.73	5.34	6.65	5.56	4.07	11.32	12.61	6.09	6.30	5.95	11.16	7.92	11.30	9.67
Nb/Nb*	0.80	0.88	0.66	0.58	0.76	0.66	0.55	0.81	0.77	0.73	0.64	0.56	0.58	0.62	0.55
Nb/U	47.30	51.00	34.00	34.92	43.13	34.46	41.50	59.00	37.24	45.85	36.54	31.58	67.84	59.69	22.64
Ce/Pb	9.56	9.49	18.77	11.76	20.34	12.02	7.51	28.41	24.53	15.27	16.45	8.05	26.96	25.40	5.31
(Nb/La)$_{PM}$	0.52	0.52	0.43	0.35	0.45	0.44	0.28	0.33	0.44	0.40	0.36	0.34	0.25	0.23	0.40
Nb/Th	10.51	12.36	8.50	7.96	10.59	8.39	9.22	16.50	11.49	11.25	9.69	7.58	11.36	14.36	6.42
La/Sm	5.32	5.85	3.76	4.05	5.49	5.92	2.96	4.50	3.47	3.45	2.68	4.42	6.31	5.59	5.91
(Nb/Th)$_{PM}$	1.25	1.47	1.01	0.95	1.26	1.00	1.10	1.97	1.37	1.34	1.16	0.90	1.35	1.71	0.76
(Th/Yb)$_{PM}$	9.00	8.70	7.57	5.09	13.09	16.76	2.65	3.23	5.40	3.45	2.71	7.25	7.68	3.82	16.34
Th/Yb	1.55	1.50	1.30	0.88	2.26	2.89	0.46	0.56	0.93	0.60	0.47	1.25	1.32	0.66	2.82
Nb/Yb	16.31	18.55	11.09	6.98	23.88	24.24	4.22	9.18	10.69	6.70	4.52	9.48	15.03	9.46	18.07
La/Ba	0.02	0.02	0.05	0.03	0.05	0.06	0.02	0.05	0.04	0.03	0.03	0.02	0.05	0.04	0.02
La/Nb	1.87	1.84	2.26	2.73	2.13	2.20	3.46	2.88	2.20	2.42	2.69	2.80	3.87	4.25	2.43
Zr/Y	12.12	15.20	7.48	9.02	13.03	15.12	5.56	3.26	6.58	6.35	6.70	10.64	12.24	7.24	23.68
Dy/Yb	2.72	2.45	3.10	2.68	3.48	3.55	3.03	3.04	3.25	2.61	2.73	2.75	3.32	3.02	2.32
La/Yb	30.45	34.05	25.11	19.08	50.83	53.22	14.61	26.42	23.56	16.18	12.19	26.50	58.20	40.15	43.94
(Hf/Sm)$_{PM}$	0.87	1.01	0.55	0.84	0.68	0.79	0.62	0.31	0.53	0.70	0.74	0.75	0.66	0.45	1.19
(Ta/La)$_{PM}$	0.65	0.67	0.44	0.41	0.48	0.49	0.33	0.29	0.46	0.42	0.42	0.40	0.21	0.19	0.40
(Hf/Sm)$_N$	0.86	1.01	0.54	0.83	0.68	0.79	0.62	0.31	0.53	0.70	0.74	0.75	0.66	0.45	1.19
(Nb/La)$_N$	0.52	0.52	0.43	0.35	0.45	0.44	0.28	0.33	0.44	0.40	0.36	0.34	0.25	0.23	0.40
Th/La	0.05	0.04	0.05	0.05	0.04	0.05	0.03	0.02	0.04	0.04	0.04	0.05	0.02	0.02	0.06
Ce/Pb	0.38	0.38	0.75	0.47	0.81	0.48	0.30	1.14	0.98	0.61	0.66	0.32	1.08	1.02	0.21
(Gd/Yb)$_{PM}$	3.14	3.35	4.18	3.07	5.43	4.87	3.07	3.93	4.32	3.13	3.06	3.16	4.65	4.26	3.03
(La/Sm)$_{PM}$	3.44	3.78	2.43	2.62	3.55	3.83	1.91	2.91	2.24	2.23	1.73	2.85	4.08	3.61	3.82
(La/Yb)$_N$	21.84	24.42	18.01	13.68	36.46	38.17	10.48	18.95	16.90	11.61	8.74	19.01	41.75	28.80	31.52
Ce/Ce*	0.97	0.98	1.00	1.00	1.00	1.00	0.98	1.01	1.03	1.02	1.00	0.97	0.99	1.03	0.93
Eu/Eu*	1.49	1.55	1.14	1.32	1.14	1.19	1.40	1.11	1.08	1.19	1.11	1.66	1.08	1.18	1.35

Note: PM denotes normalization to primitive mantle values of Sun & McDonough (1989), while N denotes normalization to chondrite values of Sun & McDonough (1989); TFe$_2$O$_3$ = total Fe$_2$O$_3$; Nb/Nb* = Nb$_{PM}$/$\sqrt{Th_{PM} \times La_{PM}}$; Ce/Ce* = Ce$_N$/$\sqrt{La_N \times Pr_N}$; Eu/Eu* = Eu$_N$/$\sqrt{Sm_N \times Gd_N}$; Troc – troctolite; Fgg – fine-grained gabbro; Ganor – gabbroic anorthosite; Norg – noritic gabbro; Gabdo – gabbrodiorite.
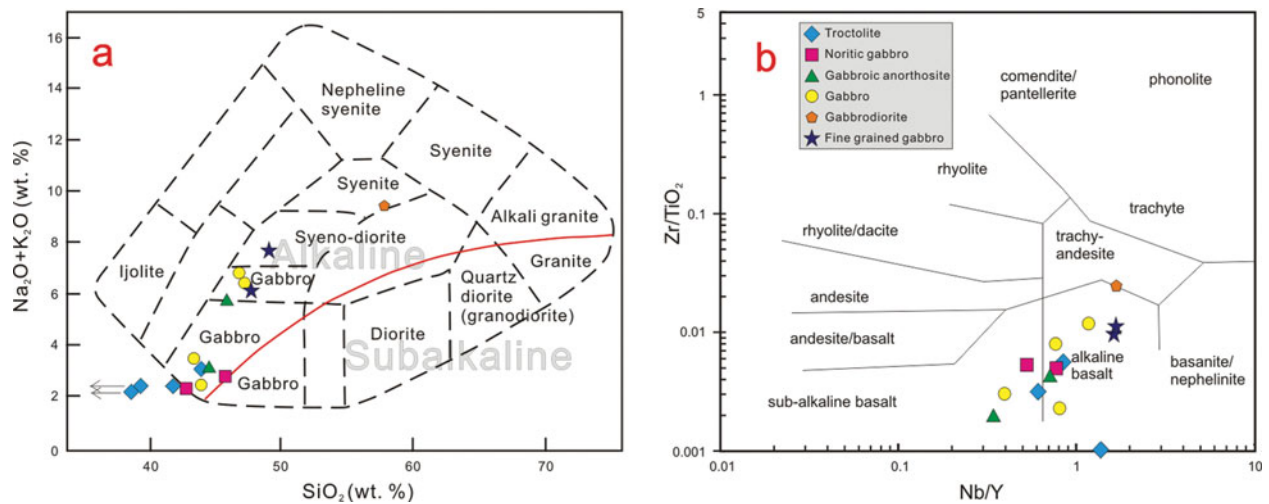
Figure 10. (Colour online) Variation diagrams of major and trace elements from the samples from the Shangzhuang intrusion. (a) $Na_2O + K_2O$ (wt %) versus SiO_2 (wt %) plot. (b) Zr/TiO_2 versus Nb/Y classification diagram. The fields in (a) are from Wilson (1989) and in (b) from Winchester & Floyd (1976).

petrogenetic interpretations. Low loss on ignition values (< 2.02 wt %) for these rocks and the lack of correlation with mobile elements, such as K, Na, Ca and Rb, suggest that the possible alteration in these samples is negligible. In addition, their limited Ce anomalies within the range of 0.90–1.03 and the high degree of other elemental correlation with the least mobile Zr on binary diagrams with a coefficient (R) > 0.75 (figure not shown) further confirm the negligible post-magmatic alteration (Polat & Hofmann, 2003).

5.d.2. Major and trace elements

Two types of troctolites can be distinguished according to their major element contents. The samples from the bottom of the intrusion exhibit moderate variations in SiO_2 (30.99–34.17 wt %), Al_2O_3 (12.12–12.21 wt %), TFe_2O_3 (28.60–32.40 wt %), TiO_2 (4.11–5.04 wt %), MgO (11.65–12.43 wt %), CaO (3.86–4.39 wt %), Na_2O (1.89–1.97 wt %) and K_2O (0.44–0.49 wt %), whereas those from the upper domain display relatively high contents of SiO_2 (41.78–44.00 wt %) and CaO (8.09–9.32 wt %), but conspicuously low TFe_2O_3 (15.63–15.66 wt %) and TiO_2 (1.62–2.13 wt %), with a large variation in Al_2O_3 (7.70–14.33 wt %), MgO (9.87–19.5 wt %), Na_2O (1.69–2.54 wt %) and K_2O (0.60–0.79 wt %) contents. The noritic gabbros and gabbroic anorthosite samples exhibit similar contents of SiO_2 (42.82–46.00 wt %), TFe_2O_3 (11.94–14.27 wt %), TiO_2 (1.35–2.51 wt %), CaO (8.87–10.95 wt %), K_2O (0.53–1.33 wt %) and Na_2O (1.67–4.46 wt %), but show a difference in Al_2O_3 (noritic gabbros: 8.76–13.58 wt %; gabbroic anorthosites: 16.50–16.76 wt %) and MgO (noritic gabbros: 11.06–16.97 wt %; gabbroic anorthosites: 4.82–6.51 wt %), which could be a reflection of the variation in the modal proportion of orthopyroxene and plagioclase. The gabbros show limited variations in SiO_2 (43.42–47.37 wt %) and TiO_2 (2.19–2.66 wt %),

and moderate variations in Al_2O_3 (10.77–16.73 wt %), TFe_2O_3 (12.04–16.50 wt %), MgO (5.24–9.96 wt %), CaO (7.54–12.49 wt %), Na_2O (1.99–4.42 wt %) and K_2O (0.55–2.38 wt %). Compared to the gabbros, the gabbrodiorite exhibits high contents of SiO_2, Al_2O_3, Na_2O and K_2O at 58.28 wt %, 17.91 wt %, 5.45 wt % and 3.90 wt %, respectively, while having low contents of TiO_2 (1.12 wt %) TFe_2O_3 (5.72 wt %), MgO (2.01 wt %) and CaO (3.7 wt %). The fine-grained gabbros exhibit very similar content of SiO_2 (47.91–49.27 wt %) and TiO_2 (2.32–2.42 wt %), and moderate variations in Al_2O_3 (15.30–15.32 wt %), TFe_2O_3 (11.65–12.66 wt %), MgO (4.36–4.96 wt %), CaO (6.36–7.06 wt %), Na_2O (4.73–4.74 wt %) and K_2O (1.38–2.94 wt %). In the TAS plot (Fig. 10a), these rocks fall in the alkaline field. In terms of the Zr/TiO_2–Nb/Y relationship (Fig. 10b), the rocks are plotted in the trachy-andesite and sub-alkaline to alkaline basalt field. Both these features emphasize their alkaline affinity.

All these rocks exhibit similar patterns in the chondrite-normalized REE diagram (Fig. 11), with relative enrichment in LREEs (light rare earth elements) compared to HREEs (heavy rare earth elements). The troctolite samples from the bottom layer exhibit total REE abundances lower than the samples from the higher domain (Fig. 11a), and show relatively high positive Eu anomalies with values in the range of 1.49–1.55 compared to 1.14–1.32. Their $(La/Yb)_N$ ratios are in the range of 21.84–24.42 and 13.68–18.01, respectively. The noritic gabbro and gabbroic anorthosite samples exhibit relatively flat patterns when compared to troctolites, with $(La/Yb)_N$ ratios ranging from 10.48 to 18.95 and positive Eu anomalies varying from 1.08 to 1.40 (Fig. 11b). The gabbro samples can be classified into two groups, following their different locations. The gabbros adjacent to the gabbrodiorite exhibit parallel and overall elevated patterns with the gabbrodiorite, and both rock types display high
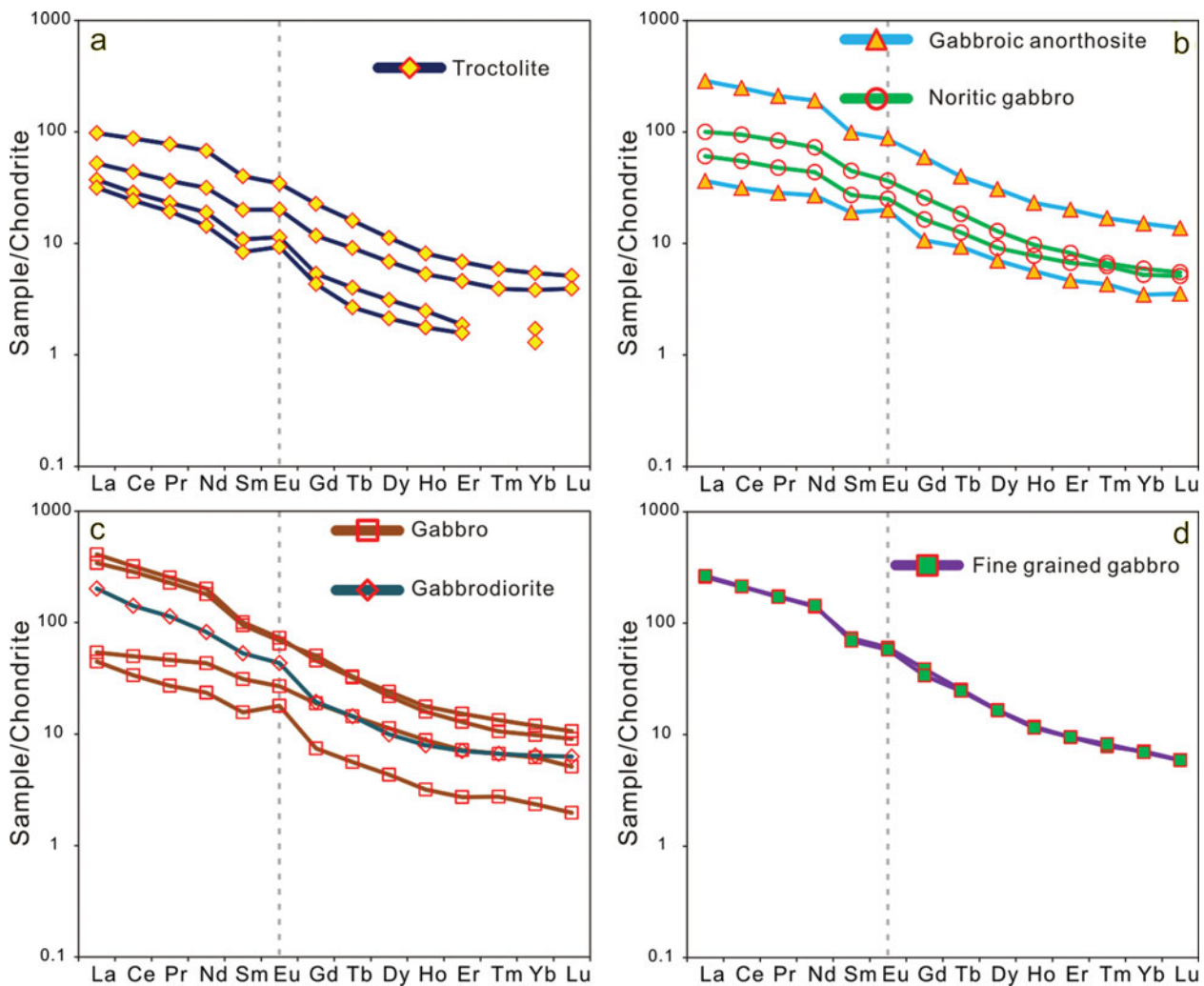
Figure 11. (Colour online) Chondrite-normalized REE patterns for (a) troctolites, (b) noritic gabbros and gabbroic anorthosites, (c) gabbros and gabbrodiorite and (d) fine-grained gabbros. Chondrite values are from Sun & McDonough (1989).

$(La/Yb)_N$ ratios in the range of 28.80–41.75, whereas the gabbros from the lower layer display comparable flat patterns with $(La/Yb)_N$ ratios varying from 8.74 to 19.01. Both the gabbros and gabbrodiorite are characterized by positive Eu anomalies with values ranging from 1.08 to 1.66 (Fig. 11c; Table 2). The fine-grained gabbro samples exhibit similar LREE concentrations but with minor differences in HREEs and $(La/Yb)_N$ ratios in the range of 36.46–38.17, accompanied by positive Eu anomalies (1.14–1.19) (Fig. 11d).

On spider diagrams normalized to primitive mantle (Fig. 12), the Shangzhuang rocks exhibit enrichment in large-ion-lithophile elements (LILEs), relative to high-field-strength elements (HFSEs). Two distinct distribution patterns can be distinguished. Two troctolites, one gabbroic anorthosite, one noritic gabbro, the gabbrodiorite and two gabbros exhibit similar patterns with peaks at Ba, K, Pb, Sr and Ti and nadir at Ce and Pr, coupled with overt Th–U and Nb–Ta 'troughs' relative to LILEs, and a Zr–Hf concave pattern relative to LREEs. The other samples (two troctolites, one gabbroic anorthosite, one noritic gabbro, two gabbros and two fine-grained gabbros) exhibit similar patterns char-

acterized by peaks at Ba, K, Pb and Sm and nadir at Ce, Pr and P, coupled with an overall La–Nd convex pattern with conspicuous troughs at Th–U and Zr–Hf. The behaviour, especially for the Ti patterns for different samples, is considered to be controlled by the modal proportion of Fe–Ti oxide.

6. Discussion

6.a. Evaluation of parent magma and differentiation

Given the close relationship between different lithologies within the Shangzhuang intrusion and their broadly comparable U–Pb ages (Figs 7, 8) as well as similar Hf isotopic compositions (Table 1, Fig. 9), we infer that these rocks share a common parent magma or were generated from similar sources.

It is difficult to precisely estimate the primary parent magma of the Shangzhuang intrusion owing to the fact that the intrusive rocks are silicate oxide mineral cumulates. Unlike other Early Cretaceous gabbros from the eastern NCC, which exhibit conspicuous negative Nb, Ta and Ti anomalies (Xu *et al.* 2004*a,b*; Huang,
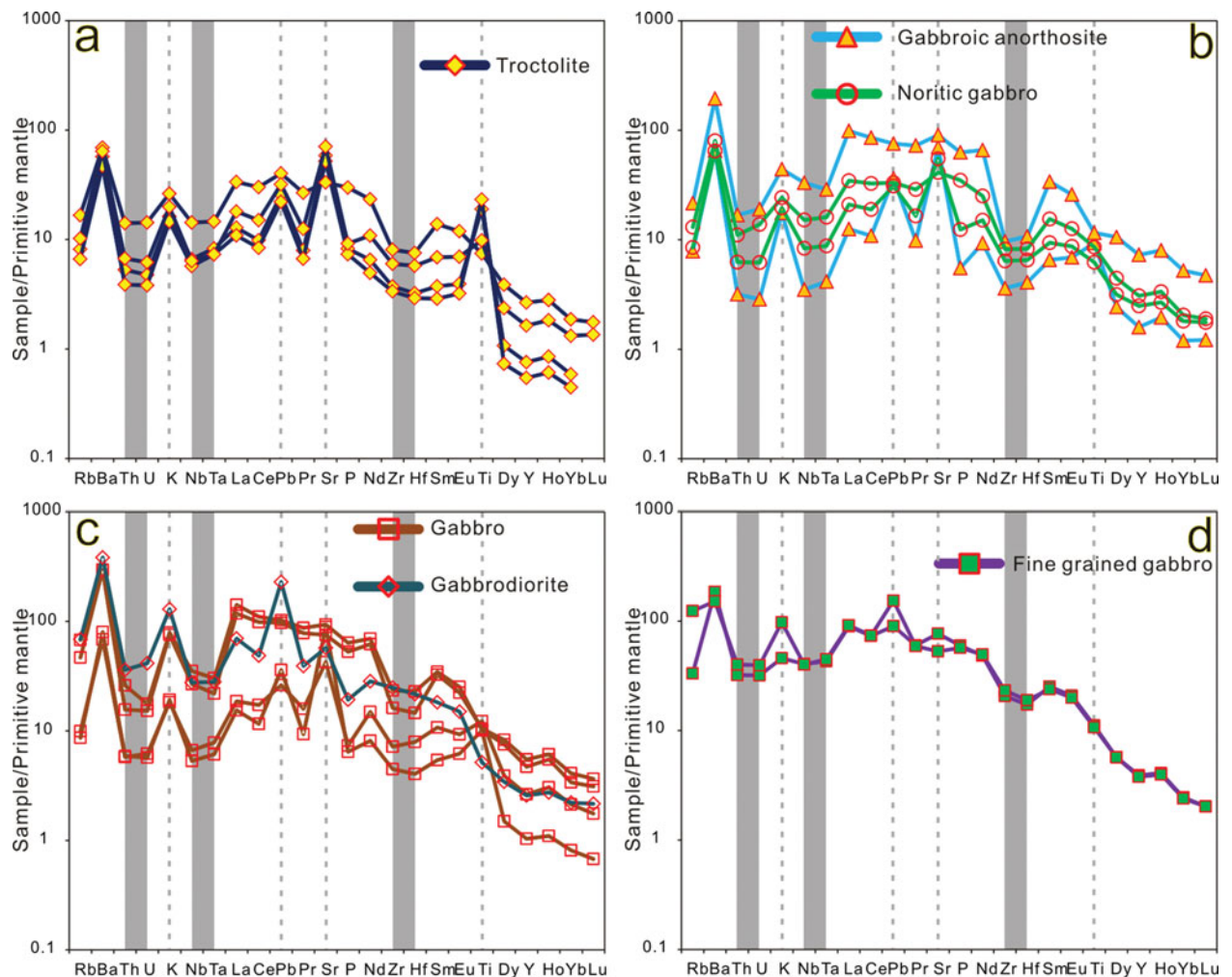
Figure 12. (Colour online) Primitive mantle-normalized variation diagrams for (a) troctolites, (b) noritic gabbros and gabbroic anorthosites, (c) gabbros and gabbrodiorite and (d) fine-grained gabbros. Primitive mantle values are from Sun & McDonough (1989).

Zhong & Xu, 2012; Xie *et al.* 2015), the Shangzhuang intrusion exhibits positive Ti anomalies and trifling negative Nb–Ta anomalies (Fig. 12), indicating Ti enrichment in the parent magma. At the same time, the presence of abundant Fe–Ti oxide minerals in different rock units suggests possible high TFe$_2$O$_3$ contents in the parent magma the same as the enrichment in Ti (Liu *et al.* 2015; Teng *et al.* 2016). In addition, high TiO$_2$ contents in hornblende and clinopyroxene and the common occurrence of ilmenite exsolution lamellae from orthopyroxene, magnetite and spinel, as well as the presence of magnetite exsolution lamellae in orthopyroxene and spinel, further suggest that these cumulus minerals were crystallized from Fe–Ti-rich melts (Teng *et al.* 2016). The Fo content of the most primitive olivine in this intrusion is ∼70–75 mol. % (Teng *et al.* 2016), indicating possible Mg enrichment in the parent magma. On the other hand, the Fo content of the olivine is notably lower than that of olivine crystallizing from a primary mantle-derived magma (Fo > 90 mol. %). The low Ni content in olivine and low Cr content in magnetite (Teng *et al.* 2016) further indicate that the Shangzhuang intrusion formed by fractiona-

tion. Usually, amphibole and mica are water-bearing minerals, and especially, amphibole is the product of incongruent melting that was triggered by a water-fluxed melt regime (Slagstad, Jamieson & Culshaw, 2005; Berger *et al.* 2008). Thus, the presence of water-bearing minerals including the euhedral magmatic amphibole (Fig. 4d) and phlogopite (Fig. 4b) that are nearly coeval with the formation of cumulate olivine and plagioclase suggest that the primary magma was hydrous. In summary, the parent magma of the Shangzhuang layered intrusion was rich in Ti, Mg and Fe, and hydrous. The concentrations of incompatible trace elements in the parent magma can be estimated by using the average composition of common cumulus mineral crystals in the most primitive lithological units and available experimental mineral/liquid partition coefficients (Roeder & Emslie, 1970; Hart & Dunn, 1993; Hauri, Wagner & Grove, 1994; Foley *et al.* 1996). In this study, owing to lack of trace-element data for the minerals, it is not possible for us to evaluate the trace elemental signature of the parent magma. The fine-grained gabbro samples could be chemically equivalent to the parent components based on the following

lines evidence. (1) The fine-grained gabbro exhibits a chilled phase when in contact with the country rocks. (2) The emplacement age of the fine-grained gabbro is defined as 127.01 ± 0.45 Ma, broadly identical to other lithologies, excluding it as a later intrusion. (3) Similar Hf isotopes in the zircons suggest the same source. (4) Compared to the Fe–Ti oxide-rich layers, the fine-grained gabbro samples exhibit higher SiO_2 contents, indicating that it was formed by vertical injection during the ascent of the magma chamber before significant differentiation occurred, rather than as residual melts after differentiation with low silica contents. These fine-grained gabbro samples are mainly composed of amphibole and plagioclase, with interstitial Fe–Ti oxides (Fig. 4k); they are chemically identical to Fe-rich basalts (Fig. 10a, b) with SiO_2 and TFe_2O_3 in the range of 47.91–49.27 wt % and 11.65–12.66 wt %. Their high TiO_2 (2.32–2.42 wt %) and MgO (4.36–4.96 wt %) contents are also in accordance with the enrichment in Ti and Mg as inferred above.

The conspicuous layered sequence of the Shangzhuang intrusion and varied proportion of minerals in different lithologies is the result of crystal sorting and accumulation, followed by differentiation, which are typical formation mechanisms for gabbros from basaltic melts (Wager & Brown, 1968; Irvine, 1979; Smith *et al.* 1983; Sisson, Grove & Coleman, 1996). In these lithologies, the ubiquitous presence of euhedral to subhedral minerals including high-Mg no. olivine and plagioclase were the first batch of products to form as cumulates from the magma, as evidenced by their euhedral crystal morphology in different lithologies (Fig. 4), marked positive correlation between MgO and Ni, and negative correlation between MgO and Al_2O_3 (Fig. 13a, b). As the plagioclase laths are less dense than olivine grains and form from relatively evolved parent magma after the extraction of already crystallized minerals, they tend to float on the roof of the magma chamber by buoyancy (Morse, 1968; Emslie, 1985). Because of their higher density, the olivine grains are more likely to contact with the liquid, and reaction of SiO_2-enriched melts with olivine results in the formation of orthopyroxene, which would explain the discrete crystals or rims mantling the olivine grains (Fig. 4b). The gravitational separation of plagioclase and olivine and the formation of orthopyroxene would make the magma much denser and more mafic because of the depletion in CaO, MgO, Al_2O_3 and SiO_2 and the enrichment of heavier components such as TiO_2, FeO and Fe_2O_3. The total iron content of the melt increases along the tholeiitic fractionation trend as experimentally illustrated by Grove & Baker (1984). Thus, Fe–Ti-rich residual magma would produce magnetite, ilmenite and titano-magnetite as later cumulus oxide minerals. However, owing to the variable modal proportions of these oxide minerals, the correlation trends between MgO and TiO_2, between MgO and TFe_2O_3, and between MgO and vanadium (V) (Fig. 13c, d, e) are not well defined. Anyhow, the broad positive cor-

relations between MgO and TiO_2, between MgO and TFe_2O_3, and between MgO and V all indicate the fractional crystallization of the first batch cumulates, especially olivine. The large scattered trend between MgO and P_2O_5 (Fig. 13f) indicates the fractionation of apatite was not significant, which is different from layered intrusions containing cumulate nelsonites (Darling & Florence, 1995; Dymek & Owens, 2001; Charlier *et al.* 2008; Tollari *et al.* 2008; Chen, Zhou & Zhao, 2013). The further evolved residual magma system would attain a new equilibrium and lead to the crystallization of Na-rich plagioclase, amphibole and phlogopite.

6.b. Assessment of crustal contamination

Contamination of crustal materials is crucial for magmas during ascent or solidification of mantle-derived melts within continental crust, especially in the case of ultramafic–mafic layered intrusions (Campbell, 1977; Kinnaird *et al.* 2002). Relatively low Th/Ta (<1.85), Ba/Zr (<5.56) and high Nb* (($Nb/Nb^* = Nb_{PM}/\sqrt{(Th_{PM} \times La_{PM})}$ (normalized to primitive mantle) $= >0.66$) anomaly values of the fine-grained gabbro samples from the Shangzhuang intrusion indicate limited crustal contamination. The ratios of Nb, Th, La, Sm and Y have been utilized as proxies for assessing crustal contamination in different settings (e.g. Wallace, Jowitt & Saleem, 2015; Santosh *et al.* 2016). Magmas originating at depth and which are influenced by crustal contamination during ascent should show a hyperbolic trend, during their passage through lower continental crust to upper continental crust. However, the behaviours of the Shangzhuang samples (non-hyperbolic trend and especially narrow variation in the ratios for the fine-grained gabbro samples) as shown in Figure 14 exclude any significant role of crustal contamination. The enrichment of the fine-grained gabbro samples would be better interpreted as the influence of the magma source region at depth rather than processes in the magma chamber at the sites of ascent and final emplacement. The negligible contamination could also be evidenced by the broadly identical Lu–Hf isotopic compositions of the different lithologies in this intrusion (Fig. 9; Table 1), suggesting the homogeneous nature of the magma.

6.c. Source nature of the Shangzhuang intrusion

The ratios of highly incompatible trace elements, such as Th, La, Ba and Nb, show only limited variation for moderately evolved magma under various petrogenetic processes such as partial melting or fractional crystallization, and are therefore particularly useful as sensitive proxies to differentiate between the contribution of convecting and non-convecting parts of the mantle to the sources of basaltic rocks (Saunders *et al.* 1992; Peate, 1997; Jourdan *et al.* 2007). For example in the Th/Yb versus Nb/Yb plot illustrated in Figure 15a, rocks from the Shangzhuang intrusion fall
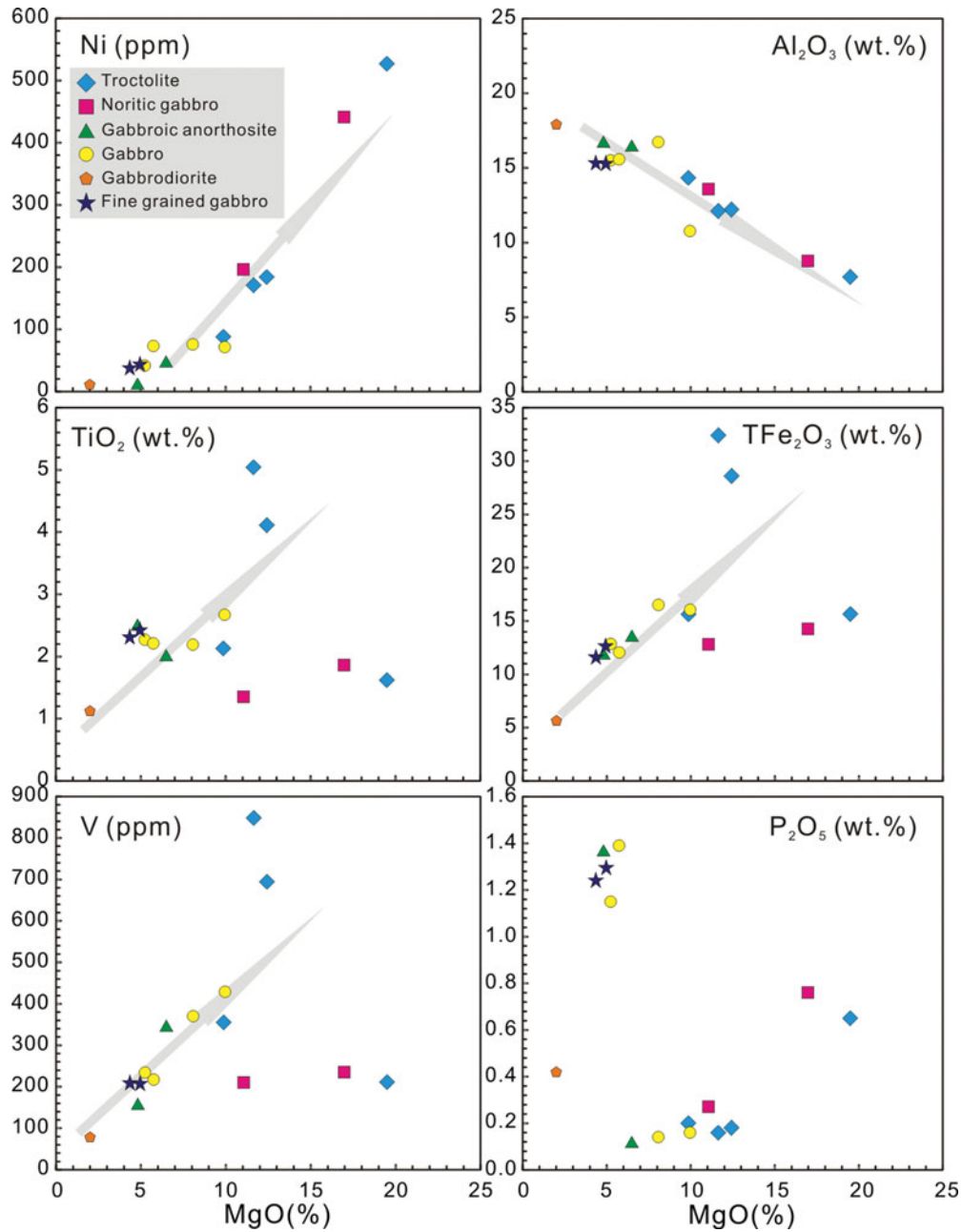
Figure 13. (Colour online) Co-variation diagrams against MgO (as fractionation index) for rocks from the Shangzhuang intrusion as follows: (a) Ni, (b) Al_2O_3, (c) TiO_2, (d) TFe_2O_3, (e) V and (f) P_2O_5.
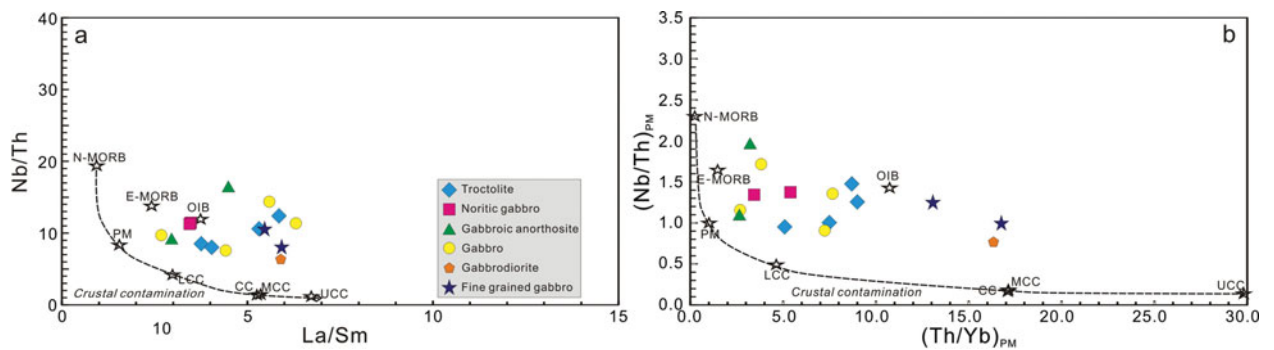
Figure 14. (Colour online) Diagrams showing variations in (a) Nb/Th and La/Sm, and (b) $(Nb/Th)_{PM}$ and $(Th/Yb)_{PM}$ for the samples analysed in this study. PM denotes normalization to primitive mantle values of Sun & McDonough (1989), with N-MORB (N-type mid-ocean ridge basalt), E-MORB (E-type mid-ocean ridge basalt) and OIB (oceanic island basalt) compositions also from Sun & Mc-Donough (1989). The upper continental crust (UCC), middle continental crust (MCC) and lower continental crust (LCC) compositions are from Rudnick & Gao (2003).
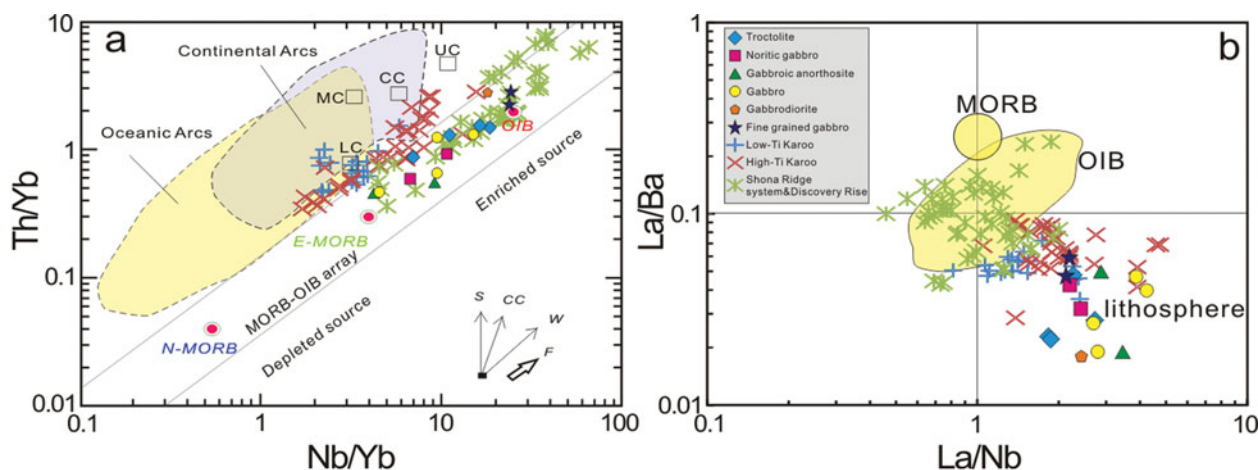
Figure 15. (Colour online) Trace-element plots of (a) Th/Yb v. Nb/Yb and (b) La/Ba v. La/Nb from rocks from the Shangzhuang intrusion. In (a), the shaded areas for oceanic arcs and continental arcs are from Wilson (2001); N-MORB, E-MORB and OIB average values are from Pearce (2008). Abbreviations: s – subduction component vector; cc – crustal contamination vector; w – within-plate variation; f – fractional crystallization; LC – lower crust; MC – middle crust; UC – upper crust; CC – continental crust. All the crustal values are from Rudnick & Gao (2003). The field in (b) is from Saunders *et al.* (1992). The geochemical data on the Shona Ridge system and Discovery Rise rocks is from Le Roex *et al.* (2010), while rocks of the Karoo LIP with high-Ti and low-Ti were compiled from Jourdan *et al.* (2007) and Neumann *et al.* (2011), respectively.

along the MORB–OIB mantle array from E-MORB to OIB with parent-equivalent fine-grained gabbros plotted near to OIB average values, exhibiting an enriched source. The higher Th/Yb ratios are likely attributed to the conservative behaviour of Yb in the subducted slab, but addition of Th and LREEs from the slab to the wedge (Pearce, 2008). Overall, their distribution patterns in Figure 15a are similar to rocks from the Shona Ridge system and Discovery Rise (Le Roex *et al.* 2010), exhibiting limited crustal contribution to the source origin, and are distinct from the basaltic rocks from the Karoo large igneous province (LIP) with crustal input in the source origin (Jourdan *et al.* 2007; Neumann *et al.* 2011). The trends of the rocks shown in Figure 15a also follow the vector of within-plate variation and fractional crystallization, and further indicate possible magma differentiation and crystal sorting as discussed above. The plots of La/Ba versus La/Nb (Fig. 15b) are located in the area towards the lithosphere with the fine-grained gabbro samples exhibiting more affinity to OIB. This inference is also corroborated by Nb/U and Ce/Pb ratios of the fine-grained gabbro samples, which are in the range of 34.46–43.13 and 12.02–20.34, respectively, showing remarkable similarity with those of OIB (Nb/U $\sim$47 $\pm$ 10; Ce/Pb $\sim$25 $\pm$ 5; Hofmann *et al.* 1986; Hofmann, 1988; Sun & McDonough, 1989), and suggest interaction of asthenospheric mantle or deeper-mantle materials with lithospheric mantle components. In summary, the rocks have an enriched mantle origin with limited crustal input. The enriched source region for the parent magma also is also supported by the $\varepsilon_{Hf}(t)$ values as illustrated in Figure 9. Since the crustal input is limited, we infer that the enriched SCLM under the NCC was stable, at least during the formation of the Shangzhuang intrusion and in the interior domain beneath the craton.

6.d. Mechanism of generation of the parent magma

Several models have been proposed for the petrogenesis of Fe-rich rocks including the following: (1) high-degree partial melting of a refractory subducted slab at low pressure (Leybourne, Van Wagoner & Ayres, 1999); (2) direct inheritance from a high-Fe mantle source, such as involvement of subducted Fe–Mn nodules (Baker & Krogh Jensen, 2004) or mantle plume-related Fe-rich streaks (Kerrich *et al.* 1999; Gibson, Thompson & Dickin, 2000); (3) low-degree partial melting of the mantle at high pressure (Hirose & Kushiro, 1993; Lassiter & DePaolo, 1997).

The possibility of formation of the Fe-rich magmas from a refractory subducted slab source at low pressure seems impossible, because of the absence of positive Nb and Ta anomalies in the Shangzhuang parent fine-grained gabbros (Fig. 12d). If Fe-rich magmas were derived from a refractory subducted slab source, positive Nb, Ta and Ti anomalies are expected (Leybourne, Van Wagoner & Ayres, 1999). The subsequent injection of subducted Fe–Mn nodules into the mantle is another possible method for Fe enrichment in SCLM (Baker & Krogh Jensen, 2004). However, process like this would also lead the magma to be Mn enriched (Ichiyama *et al.* 2006), which is not in accordance with the low MnO content in the present case (Table 2). The model of direct inheritance from mantle plume-related Fe-rich streaks should be reflected in high positive zircon anomalies $\varepsilon_{Hf}(t)$ and $(Nb/La)_{PM}$ (>1, Gibson, 2002), obviously different from the negative zircon $\varepsilon_{Hf}(t)$ (Fig. 9; Table 1) and parent-equivalent fine-grained gabbros with $(Nb/La)_{PM}$ less than 0.5 (Table 2) in the present case. Combined with the enriched nature as shown in Figure 15, we exclude this model. The third scenario for the Shangzhuang intrusion is related to low-degree partial melting of the mantle at high

pressure. Alternatively, the potential mantle source for high-Fe mafic melts includes eclogite foundered lower crust, and pyroxenite- and lherzolite-rich mantle. Experimental studies of Klemme, Blundy & Wood (2002) showed that melt derived from the eclogitic lower crust would have low MgO and high SiO_2 and Al_2O_3, CaO/Al_2O_3 and Ni/MgO (Sobolev *et al.* 2005; Spandler *et al.* 2008), which is in contrast to the features of the Shangzhuang rocks, especially with the fine-grained gabbro considered to represent the composition of the early melt. The same also applies to partial melts derived from mantle pyroxenite (without olivine), which would generate magmas with high Ni/MgO (Sobolev *et al.* 2005, Herzberg, 2006), in contrast to the low Ni/MgO in the Shangzhuang rocks. Also, experimentally simulated partial melts of garnet pyroxenite are far too aluminous to be appropriate for the Shangzhuang intrusion (Hirschmann *et al.* 2003; Kogiso, Hirschmann & Frost, 2003). Thus, the origin of the Shangzhuang intrusion is likely related to lherzolite facies mantle. Peridotite has been considered as the major mantle lithology in Mesozoic time in the NCC (Gao *et al.* 2004) and has been confirmed by the wide occurrence of Late Jurassic high-Mg andesites, dacites and adakites in the NCC where they exhibit unusual compositions that are interpreted to result from melting of ancient, mafic lower crust which was foundered into the mantle (Rudnick, 2005) and supported by the identification of peridotite xenoliths (Zheng *et al.* 2001; Rudnick *et al.* 2004; Ying *et al.* 2006; Xiao *et al.* 2010). The co-variation of Zr/Y versus TiO_2/Al_2O_3 (Fig. 16) has been utilized to estimate the pressure or melting degree of partial melting. The trend for the fine-grained gabbro samples from the Shangzhuang intrusion suggests relatively high pressure or a low degree of partial melting when compared to the Abitibi (Kerrich, Polat & Xie, 2008) and Chagangnuoer (Li *et al.* 2014*a*) high-Fe-rich basalts, the Zhongtiao Fe-rich mafic sill (Li *et al.* 2014*a*), the Ji'nan gabbro (Xie *et al.* 2015) and picrites from Iceland (Skovgaard *et al.* 2001). Their features are similar to that of Fe-rich basalts from Tarim (Jiang *et al.* 2004) and Emeishan (Xu *et al.* 2003), although lower than the ranges in Siberian basalts (Arndt, Lehnert & Vasil'ev, 1995). Besides, the equivalent fine-grained gabbros in our study exhibit relatively low values of Dy/Yb (3.48–3.55), and are plotted near the phlogopite–spinel lherzolite facies without significant garnet in the source as shown in Figure 17a (Liu *et al.* 2014) and within spinel lherzolite facies in Figure 17b (Zhu *et al.* 2009). The rocks display La abundance and La/Sm values higher than those generated by depleted- or primitive-mantle melting. The partial melting trajectory for the Shangzhuang intrusion also implies low partial melting of less than ∼5% of an enriched mantle that contains mainly spinel lherzolite (Green, 2006; Zhu *et al.* 2009). The possible mechanism of Ti and Mg enrichment in the parent magma is attributed to the addition of magmas from a deeper-mantle source, which also provided heat and additional Fe to the parent magma.

As stated in the previous section, the Shangzhuang intrusion shows negligible crustal contamination, reflecting the influence of the magma source region at depth rather than processes in the magma chamber at the site of emplacement. The fine-grained gabbros show enrichment in LILEs (e.g. Rb, K, Th and U) and moderate depletion of HFSEs (e.g. Nb, Ta, Zr and Hf) and HREEs (Fig. 12d), together with depletion of Nb and Ta relative to La (Figs 12d, 18a, b). These features suggest that the magma originated from an enriched SCLM source that had been affected by metasomatism induced by subduction (Wilson, 1989; La Flèche, Camire & Jenner, 1998; Wang *et al.* 2004), through the circulation of carbonatitic- or subduction-melts and/or fluids (Elliott *et al.* 1997; Class *et al.* 2000; Kogarko, Kurat & Ntaflos, 2001; Reubi, Sims & Bourdan, 2014). Generally, mantle-derived magmas influenced by carbonate metasomatism are ultramafic and show low $(Hf/Sm)_{PM}$ and $(Hf/Sm)_N$ values (La Flèche, Camire & Jenner, 1998; Kogarko, Kurat & Ntaflos, 2001; Gasparik & Litvin, 2002; Hammouda, 2003). Rocks from Shangzhuang intrusion exhibit high $(Hf/Sm)_{PM}$ and $(Hf/Sm)_N$ values, and therefore their mantle source was unlikely to have been metasomatized by carbonatite (Fig. 18a, b). The negligible influence on the mantle by carbonatite can also be evidenced by the absence of calcite disseminations in the Shangzhung intrusion, unlike some intrusions that have been affected by carbonatite, such as those Alaskan-type ultramafic or mafic intrusions in arc settings with calcite disseminations/a calcium-rich signature (Eyuboglu *et al.* 2010; Deng *et al.* 2015*a*; Teng, Yang & Santosh, 2015), which is also consistent with their alkaline signature other than calc-alkaline affinity (Fig. 10a, b). In the Th/La versus Ce/Pb diagram (Fig. 18c), these rocks show low Th/La ratios and plot along a trend consistent with what would be expected for slab fluid influence (Temizel *et al.* 2012); this is consistent with their behaviour in Figure 18a, b, which shows affinity to fluid-related subduction metasomatism. With the input of large-scale impregnation by fluids, partial melting of the refractory mantle would likely occur. Partial melting of the refractory mantle with a high viscosity hardly occurs, even when heated by a plume (Rudnick *et al.* 2004). Deviation of the Shangzhuang rocks from melt-related subduction and carbonatite could also attest to the negligible crustal contamination as discussed above.

6.e. Tectonic implications

The geochemical and isotopic features of the Shangzhuang intrusion do not favour arc-related magmatism where prominent imprints of melting of subducted slab should exist. The non-arc affinity of the intrusion is further strengthened by their contrast with subduction zone magmas, which exhibit large Nb–Ta depletions and minor Ti depletions, with strong enrichments in K and Pb, and lesser enrichment of Sr (Fig. 12d), plotting away from typical oceanic and continental
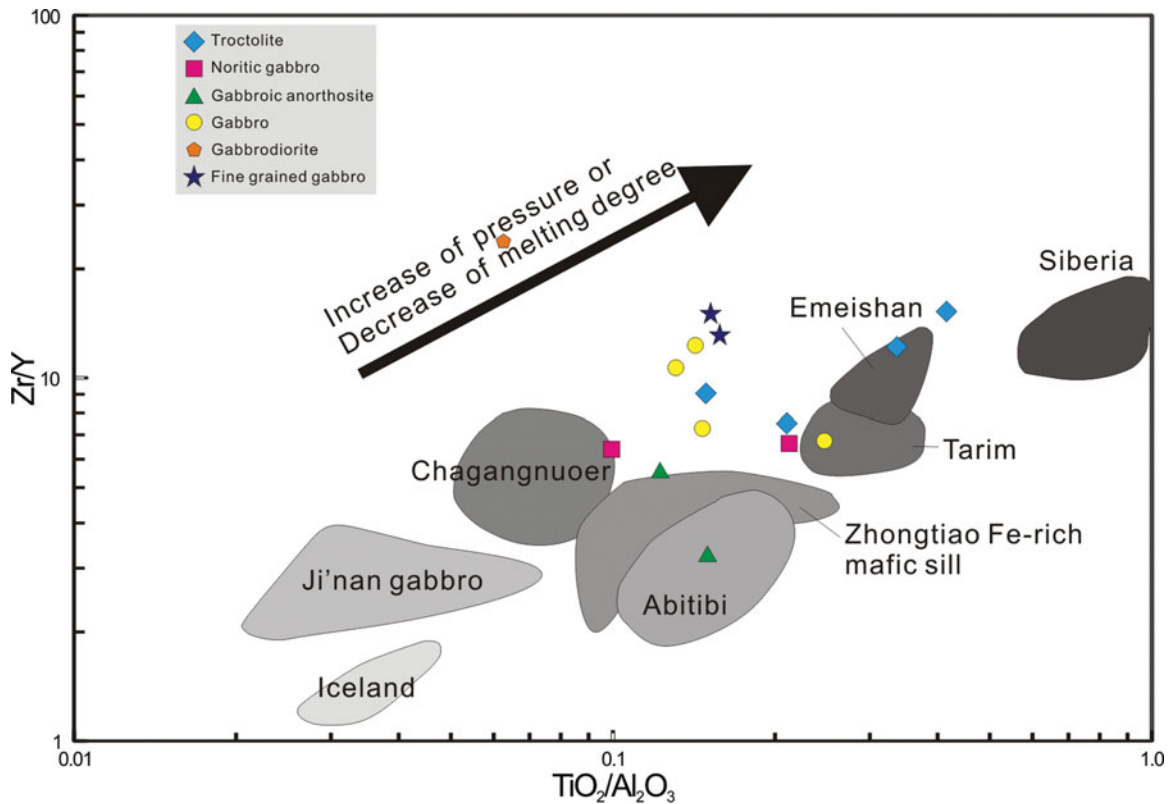
Figure 16. (Colour online) Plots of Zr/Y v. TiO_2/Al_2O_3 for the Shangzhuang rocks after Ichiyama & Ishiwatari (2005). Picrites from Iceland in the middle (Skovgaard *et al.* 2001), an Fe-rich mafic sill from the Zhongtiao Mountains (Li *et al.* 2014*a*), and Fe-rich basalts from Ji'nan gabbro (Xie *et al.* 2015), Abitibi (Kerrich, Polat & Xie, 2008), Chagangnuoer (Li *et al.* 2014*a*), Tarim (Jiang *et al.* 2004), Emeishan (Xu *et al.* 2003) and Siberia (Arndt, Lehnert & Vasil'ev, 1995) are shown for comparison.
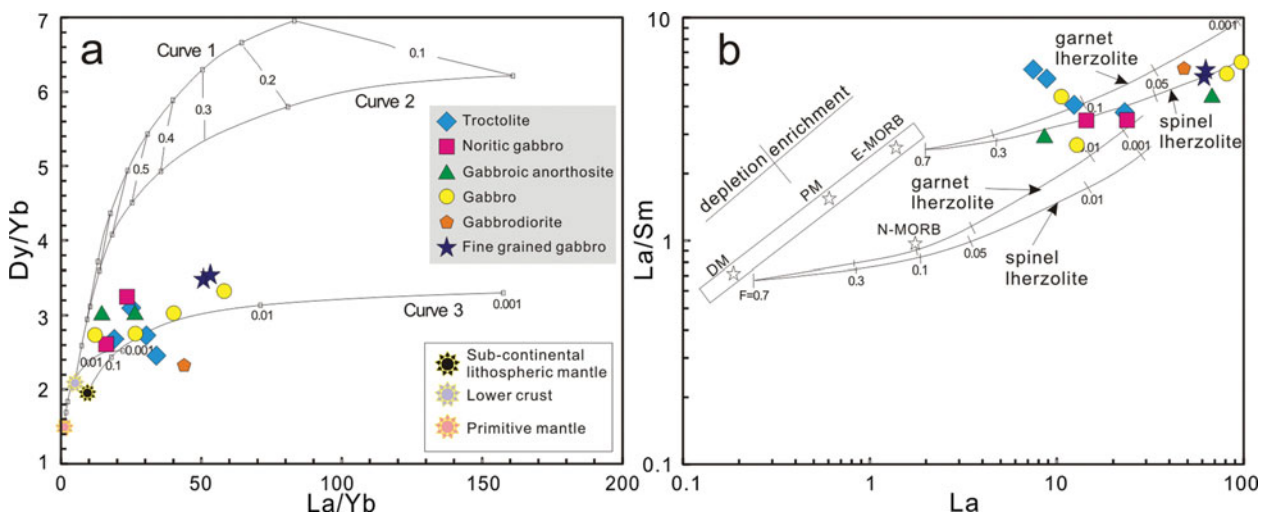
Figure 17. (Colour online) Plots of (a) Dy/Yb v. La/Yb (after Liu *et al.* 2014) and (b) La v. La/Sm for the Shangzhuang rocks (after Zhu *et al.* 2009). In (a), La, Dy and Yb concentrations of primitive mantle, sub-continental lithospheric mantle and lower crust are from Sun & McDonough (1989), McDonough (1990) and Rudnick & Gao (2003), respectively. Curve 1 and curve 2 belong to rutile-bearing eclogitic facies, composed of garnet (64 %) + clinopyroxene (35 %) + rutile (1 %) and garnet (35 %) + clinopyroxene (64 %) + rutile (1 %), respectively, while curve 3 represents phlogopite-spinel lherzolite facies, composed of olivine (70 %) + orthopyroxene (15 %) + clinopyroxene (9 %) + phlogopite (5 %) + spinel (1 %). In (b), mantle arrays defined by depleted mantle (DM; McKenzie & O'Nions, 1991), primitive mantle (PM) and E-MORB compositions (Sun & McDonough, 1989) are shown. Melting curves for spinel lherzolite are composed of olivine (53 %) + orthopyroxene (27 %) + clinopyroxene (17 %) + spinel (3 %), while garnet lherzolite is composed of olivine (60 %) + orthopyroxene (20 %) + clinopyroxene (10 %) + garnet (10 %) sources, with both DM and E-MORB compositions after Aldanmaz *et al.* (2000). Short lines on each melting curve correspond to degrees of partial melting for a given mantle source. Values in brackets denote the mineral percentages in the residue.
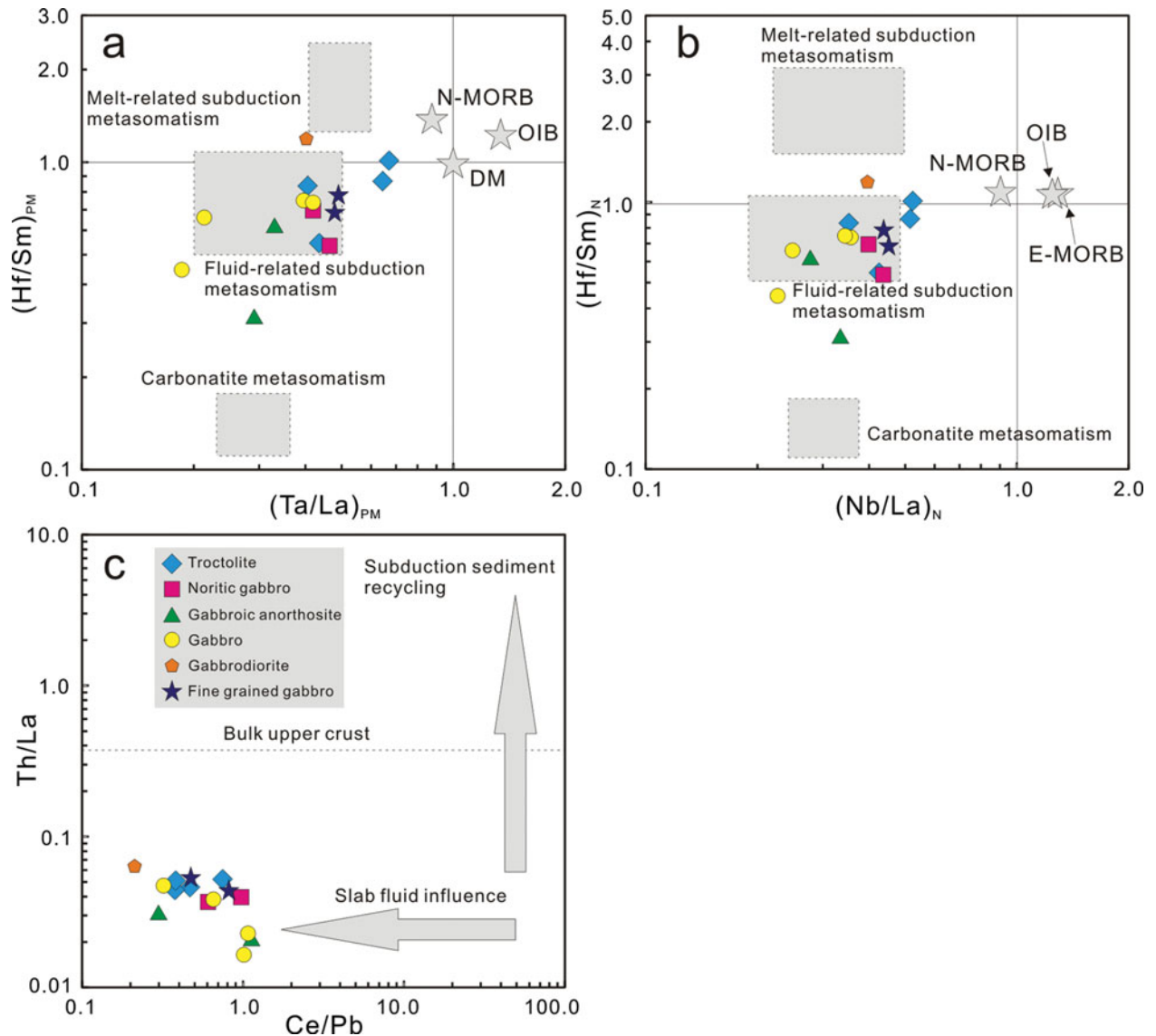
Figure 18. (Colour online) Co-variation diagrams of (a) $(Hf/Sm)_{PM}$ v. $(Ta/La)_{PM}$ and (b) $(Hf/Sm)_N$ v. $(Nb/La)_N$ (after La Flèche, Camire & Jenner, 1998); and (c) Th/La v. Ce/Pb (Temizel et al. 2012), illustrating that the source region of the Shangzhuang rocks has been influenced by subduction-related fluids.

arcs (Fig. 15a) with no prominent correlation to arc magmatism (Fig. 19). The features displayed in the present case are comparable with those of many mafic–ultramafic layered intrusions occurring within cratonic domains and correlated to extensional or rift settings (Brooks, Larsen & Nielsen, 1991; von Gruenewaldt & Harmer, 1992; Seo et al. 2013; Teng & Santosh, 2015). The parent magma of the Shangzhuang intrusion was generated through partial melting of a spinel-bearing lherzolite source in the SCLM which had been enriched by metasomatism through prolonged subduction of the Mongolian oceanic slab during Late Palaeozoic time. The culmination of subduction was marked by the final collision between the Mongolian microcontinent and the NCC in Late Permian time along the Solonker–Linxi suture zone (Chen et al. 2000; Davis et al. 2001; Xiao et al. 2003; Windley et al. 2007; Teng, Yang & Santosh, 2015). However, the contemporan-

eous subduction of the Pacific Plate beneath provided only a minor contribution to further fertilize the mantle source for the Shangzhuang magma, as shown in Figure 9, where the zircon $\varepsilon_{Hf}(t)$ values are distributed within the evolution array of the Mongolian oceanic subduction-induced enriched SCLM (Yang et al. 2006a; Chen et al. 2008; Teng, Yang & Santosh, 2015), without any obvious trend of further enrichment.

The emplacement age of the Shangzhuang intrusion is constrained as c. 128 to 123 Ma, coeval with those of other intrusive phases in Xuejiashiliang Complex at ~128.8–123.7 Ma (Su et al. 2006, 2007). Although this age for the Shangzhuang intrusion pre-dates the regional extension related to Yanshanian tectonics that widely occurred at ~118–115 Ma, which has been evidenced by the Hefangkou Fault and contemporary Yunmengshan granodiorite (118–116 Ma) and Daguikou pluton (117±2 Ma) (Davis et al.
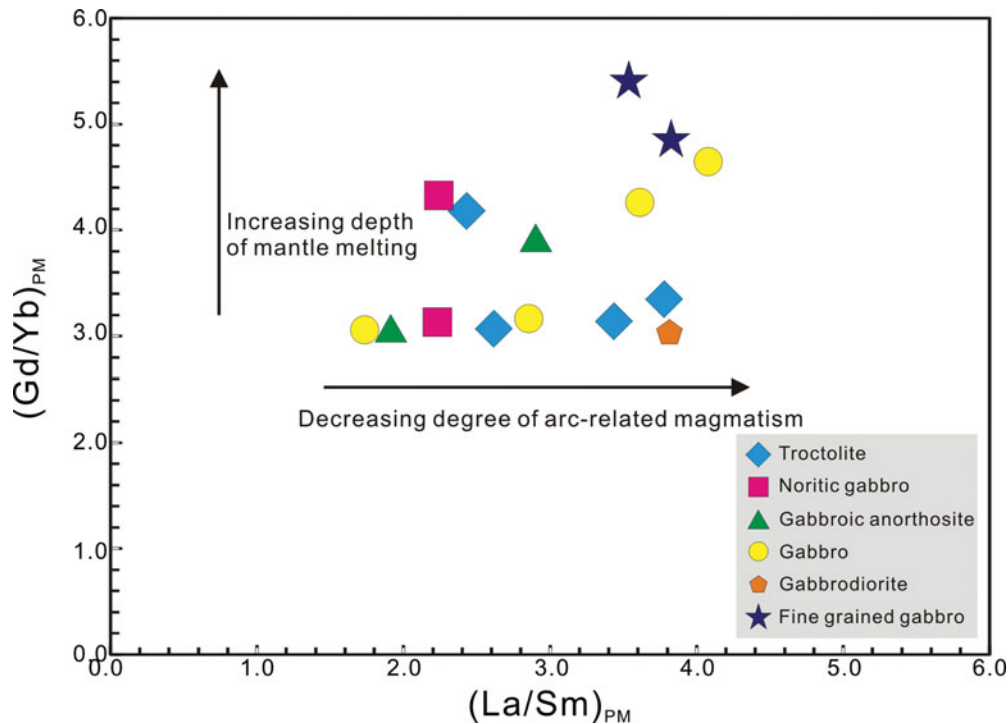
Figure 19. (Colour online) Diagram showing variations in $(Gd/Yb)_{PM}$ and $(La/Sm)_{PM}$ values (normalized to primitive mantle (PM) values of McDonough & Sun, 1995). Increasing $(Gd/Yb)_{PM}$ ratios are indicative of increasing depth of mantle melting, whereas increasing $(La/Sm)_{PM}$ ratios are indicative of decreasing influence of slab-related or crustal components or assimilation of arc-related material.

1996*a*,*b*, 2001), it is spatially consistent with the extensional setting between *c*. 135 and 115 Ma in the eastern and central NCC related to the Mesozoic lithospheric thinning beneath the craton, as demonstrated by the appearance of A-type granite, dyke swarms and structural features including metamorphic core complexes and extensional basins (Wu *et al.* 2005; Yang *et al.* 2007; Li *et al.* 2012; Wang *et al.* 2012; Gao, Zhao & Chen, 2014). Two prevalent models for the thinning of the lithospheric mantle for the NCC are thermal and/or chemical erosion of lithospheric mantle by continuous heat/materials input from deep-asthenosphere (Zhang *et al.* 2003; Xu *et al.* 2004*a*; Menzies *et al.* 2007), and rapid 'sink down' delamination/foundering from the lithospheric mantle due to density increase (Gao *et al.* 2004; Yang *et al.* 2005; Ling *et al.* 2009). In general, delamination/foundering would cause large quantities of basaltic underplating and magma ponding at the base of the crust, some of which might erupt into the surface of the crust (Deng *et al.* 2007). Zhang *et al.* (2009*b*) considered that the initiation of lithospheric thinning of the NCC might date back to Early–Late Triassic time along the northern margin of the NCC, and evolved into the interior domain gradually. Gao *et al.* (2004) considered that the large-scale lithospheric removal related to delamination/foundering started at ∼160 Ma, as evidenced by the wide occurrence of Late Jurassic high-Mg andesites, dacites and adakites in the NCC (Rudnick, 2005). Since the emplacement of the Shangzhuang intrusion was related to the intra-continental extension in the eastern and cent-

ral NCC during *c*. 135 and 115 Ma, with only sparse exposures of basaltic rocks and high-Mg andesites, dacites and adakites in the nearby area, we consider that the thermal and/or chemical erosion model is more plausible (Rudnick, 2005; Deng *et al.* 2007).

The nature of lithospheric mantle domains beneath the NCC has been well addressed through Sr–Nd–Pb isotope geochemical data from the mantle-derived volcanic rocks, mafic intrusive rocks and mantle xenoliths (Zhang *et al.* 2003, 2004; Xu *et al.* 2004*b*; Zheng *et al.* 2005; Huang, Zhong & Xu, 2012). For the lithospheric mantle beneath the eastern NCC, an EMI-like domain and EMII-like domain are distinguished along the boundary, which lies about ∼80 km west of Tan-Lu fault (Xu *et al.* 2004*b*), with the western part dominantly EMI-like. This has been correlated to the subduction of either pelagic sediments or sub-continental lithosphere, whereas the eastern part is dominantly EMII-like, and considered to represent subducted continental sediments (Hart *et al.* 1992; Hofmann, 1997) or incorporation of recycled oceanic lithosphere into the SCLM with trapped melt fractions (Workman *et al.* 2003). The Shangzhuang rocks show a non-arc signature, and recycled components played little contribution as shown in Figure 19, which is different from the EMII-like domain. Thus, the origin for the Shangzhuang rocks is more likely correlated to the EMI-like enriched mantle. However, these rocks exhibit a geochemical signature that is more complex and different from magmas derived from a typical EMI-like source, such as the Zr/Nb, Zr/Y and Nb/Y values for the fine-

grained gabbros ranging from 8.03–9.09, 13.0–15.1 and 1.62–1.66, whereas typical EMI-like mantle has a very low Zr/Nb ratio ($\sim$5) and high Zr/Y ($\sim$12) and Nb/Y ($\sim$3) ratios (Condie, 2005). We, therefore, infer that a deep-mantle source such as the asthenosphere or mantle plume also played a role in the mixing of the parent magma. The emplacement age of the Shang-zhuang intrusion corresponds well with the intra-continental extensional setting in the eastern and central NCC. The heat induced by asthenospheric mantle upwelling under intra-continental extension (Menzies, Fan & Zhang, 1993; Fan *et al.* 2000), and addition of the water derived from the ongoing subducting Pacific Plate could together reduce the solidus of the SCLM and the viscosity contrast between the lithospheric mantle and the asthenosphere, thus leading to thermal and/or chemical erosion of the SCLM which had been fertilized by the subduction process of the Mongolian oceanic slab during Late Palaeozoic time. This process is similar to a plume impinging on lithosphere but with a limited extent (Davies & von Blanckenburg, 1995), and with an ephemeral thermal anomaly (van de Zedde & Wortel, 2001) of limited extent. This could be a good interpretation for the extra enrichment in Fe, Ti and Mg in the Shangzhuang intrusion, but without the extensive depletion if large mantle plume events occurred.

7. Conclusions

(1) The Shangzhuang layered mafic intrusion was emplaced during Early Cretaceous time with its age constrained as *c*. 128–123 Ma. The timing of emplacement correlates with the major extensional setting between *c*. 135 and 115 Ma in the eastern and central NCC related to the Mesozoic lithospheric thinning.

(2) The parent magma for the Shangzhuang mafic layered intrusion was likely enriched in Fe, Ti and Mg, generated through a low (less than $\sim$5%) degree of partial melting of a spinel lherzolite source in the lithospheric mantle beneath the NCC. The geochemical and zircon Lu–Hf isotopic data suggest that the source of the Shangzhuang intrusion had been enriched by crust–mantle interaction and metasomatic fluids and melts derived from the Late Palaeozoic Mongolian oceanic subduction beneath the northern NCC. These were locally mixed with limited asthenospheric or deeper-mantle materials by mantle upwelling under the intra-continental extension related to the Mesozoic lithospheric thinning in the eastern and central NCC.

(3) The formation of the layered sequence is ascribed to crystal sorting and accumulation, followed by differentiation through density contrast and continuous re-equilibration.

(4) The tectonic setting for the formation of the Shangzhuang parent magma was considered to be intra-continental extensional that triggered mantle upwelling to provide heat/materials, leading to thermal–chemical erosion of the lithospheric mantle.

Supplementary material

To view supplementary material for this article, please visit https://doi.org/10.1017/S0016756817000371

References

ALDANMAZ, E., PEARCE, J. A., THIRLWALL, M. F. & MITCHELL, J. G. 2000. Petrogenetic evolution of late Cenozoic, post-collision volcanism in western Anatolia, Turkey. *Journal of Volcanology and Geothermal Research* **102**, 67–95.

AMELIN, Y., LEE, D. C. & HALLIDAY, A. N. 2000. Early–Middle Archaean crustal evolution deduced from Lu–Hf and U–Pb isotopic studies of single zircon grains. *Geochimica et Cosmochimica Acta* **64**, 4205–25.

ANDERSON, D. L., TANIMOTO, T. & ZHANG, Y. 1992. Plate tectonics and hotspots: the third dimension. *Science* **256**, 1645–50.

ANDERSON, T. 2002. Correction of common Pb in U–Pb analyses that do not report ^{204}Pb. *Chemical Geology* **192**, 59–79.

ARNDT, N., LEHNERT, K. A. & VASIL'EV, Y. 1995. Meimechites: highly magnesian lithosphere–contaminated alkaline magmas from deep subcontinental mantle. *Lithos* **34**, 41–59.

BAKER, J. A. & KROGH JENSEN, K. 2004. Coupled ^{186}Os–^{187}Os enrichments in the Earth's mantle–core–mantle interaction or recycling of ferromanganese crusts and nodules? *Earth and Planetary Science Letters* **220**, 277–86.

BATANOVA, V. G., PERTSEV, A. N., KAMENETSKY, V. S., ARISKIN, A. A., MOCHALOV, A. G. & SOBOLEV, A. V. 2005. Crustal evolution of island-arc ultramafic magma: Galmoenan pyroxenite–dunite plutonic complex, Koryak, Highland (Far East Russia). *Journal of Petrology* **46**, 1345–66.

BERGER, A., BURRI, T., ALT-EPPING, P. & ENGI, M. 2008. Tectonically controlled fluid flow and water-assisted melting in the middle crust: an example from the Central Alps. *Lithos* **102**, 598–615.

BLICHERT-TOFT, J. & ALBARÈDE, F. 1997. The Lu–Hf isotope geochemistry of chondrites and the evolution of the mantle–crust system. *Earth and Planetary Science Letters* **148**, 243–58.

BOYD, F. R. & GURNEY, J. 1986. Diamonds and the African lithosphere. *Science* **239**, 472–7.

BROOKS, C. K., LARSEN, L. M. & NIELSEN, T. F. D. 1991. Importance of iron-rich tholeiitic magmas at divergent plate margins: a reappraisal. *Geology* **19**, 269–72.

CAMPBELL, I. H. 1977. Study of macro-rhythmic layering and cumulate processes in Jimberlana intrusion, Western Australia. 1. Upper layered series. *Journal of Petrology* **18**, 183–215.

CAWTHORN, R. G. 1996. *Layered Intrusions [M]*. Amsterdam: Elsevier Science.

CHARLIER, B., SAKOMA, E., SAUVÉ, M., STANAWAY, K., AUWERA, J. V. & DUCHESNE, J. C. 2008. The Grader layered intrusion (Havre-Saint-Pierre Anorthosite, Quebec) and genesis of nelsonite and other Fe-Ti-P ores. *Lithos* **101**, 359–78.

CHEN, B., JAHN, B. M., WILDE, S. & XU, B. 2000. Two contrasting Paleozoic magmatic belts in northern Inner Mongolia, China: petrogenesis and tectonic implications. *Tectonophysics* **328**, 157–82.

CHEN, B., TIAN, W., JAHN, B. M. & CHEN, Z. C. 2008. Zircon Shrimp U–Pb ages and in-situ Hf isotopic analysis for the Mesozoic intrusions in South Taihang, North China craton: evidence for hybridization between mantle-derived magmas and crustal components. *Lithos* **102**, 118–37.

CHEN, W. T., ZHOU, M. F. & ZHAO, T. P. 2013. Differentiation of nelsonitic magmas in the formation of the ∼1.74 Ga Damiao Fe–Ti–P ore deposit, North China. *Contributions to Mineralogy and Petrology* **165**, 1341–62.

CLASS, C., MILLER, D. M., GOLDSTEIN, S. L. & LANGMUIR, C. H. 2000. Distinguishing melt and fluid subduction components in Umnak Volcanics, Aleutian Arc. *Geochemistry Geophysics Geosystems* **1**, 1004.

CONDIE, K. C. 2005. High field strength element ratios in Archean basalts: a window to evolving sources of mantle plumes? *Lithos* **79**, 491–504.

DARLING, R. S. & FLORENCE, F. P. 1995. Apatite light rare earth element chemistry of the Port Leyden nelsonite, Adirondack Highland, New York: implications for the origin of nelsonite in anorthosite suite rocks. *Economic Geology* **90**, 964–8.

DAVIES, J. H. & VON BLANCKENBURG, F. 1995. Slab break-off: a model of lithosphere detachment and its test in the magmatism and deformation of collisional orogens. *Earth and Planetary Science Letters* **129**, 85–102.

DAVIS, G. A., QIAN, X., ZHENG, Y., YU, H., WANG, C., TONG, H. M., GEHRELS, G. E., SHAFIQUALLAH, M. & FRYXELL, J. E. 1996a. Mesozoic deformation and deformation and plutonism in the Yunmengshan: a Chinese metamorphic core complex north of Beijing. In *The Tectonic Evolution of Asia* (eds A. Yin & T. M. Harrison), pp. 253–80. Cambridge: Cambridge University Press.

DAVIS, G. A., QIAN, X., ZHENG, Y., YU, H., WANG, C., TONG, H. M., GEHRELS, G. E., SHAFIQUALLAH, M. & FRYXELL, J. E. 1996b. The Huairou (Shuiyu) ductile shear zone, Yunmengshan Mts., Beijing. In *International Geological Congress, 30th, Field Trip Guide*. Beijing: Geological Publishing House, 25 pp.

DAVIS, G. A., ZHENG, Y. D., WANG, C., DARBY, B. J., ZHANG, C. H. & GEHRELS, G. E. 2001. Mesozoic tectonic evolution of the Yanshan fold and thrust belt, with emphasis on Hebei and Liaoning Provinces, Northern China. In *Paleozoic and Mesozoic Tectonic Evolution of Central Asia: From Continental Assembly to Intracontinental Deformation* (eds M. S. Hendrix & G. A. Davis), pp. 171–97. Geological Society of America Memoir no. 194.

DENG, J. F., SU, S. G., NIU, Y. L., LIU, C., ZHAO, G. C., ZHAO, X. G., ZHOU, S. & WU, Z. X. 2007. A possible model for the lithospheric thinning of North China Craton: evidence from the Yanshanian (Jura-Cretaceous) magmatism and tectonism. *Lithos* **96**, 22–35.

DENG, Y. F., YUAN, F., ZHOU, T., WHITE, N. C., ZHANG, D. Y., GUO, X. J., ZHANG, R. F. & ZHAO, B. 2015a. Zircon U–Pb geochronology, geochemistry, and Sr–Nd isotopes of the Ural–Alaskan type Tuerkubantao mafic–ultramafic intrusion in southern Altai orogen, China: petrogenesis and tectonic implications. *Journal of Asian Earth Sciences* **113**, 36–50.

DENG, Y. F., YUAN, F., ZHOU, T., XU, C., ZHANG, X. & GUO, X. 2015b. Geochemical characteristics and tectonic setting of the Tuerkubantao mafic-ultramafic intrusion in West Junggar, Xinjiang, China. *Geoscience Frontiers* **6**, 141–52.

DILEK, Y. & FURNES, H. 2011. Ophiolite genesis and global tectonics: geochemical and tectonic fingerprinting of ancient oceanic lithosphere. *Geological Society of America Bulletin* **123**, 387–411.

DYMEK, R. F. & OWENS, B. E. 2001. Petrogenesis of apatite-rich rocks (nelsonites and oxide-apatite gabbronorite) associated with massif anorthosite. *Economic Geology* **96**, 797–815.

ELLIOTT, T., PLANK, T., ZINDLER, A., WHITE, W. & BOURDON, B. 1997. Element transport from slab to volcanic front at the Mariana arc. *Journal of Geophysical Research* **102**, 14991–5019.

EMSLIE, R. F. 1985. Proterozoic anorthosite massifs. In *The Deep Proterozoic Crust in the North Atlantic Provinces* (eds A. C. Tobi & J. L. R. Touret), pp. 39–60. NATOASI ser C.158. Dordrecht: Reidel.

ERNST, R. E. & JOWITT, S. M. 2013. Large igneous provinces (LIPS) and metallogeny. In *Tectonics, Metallogeny, and Discovery: the North American Cordillera and Similar Accretionary Settings* (eds M. Colpron, T. Bissig, B. G Rusk & J. F. H. Thompson), pp. 17–51. Society of Economic Geologists Special Publication 17.

EYUBOGLU, Y., DILEK, Y., BOZKURT, E., BEKTAS, O., ROJAY, B. & SEN, C. 2010. Structure and geochemistry of an Alaskan-type ultramafic–mafic complex in the Eastern Pontides, NE turkey. *Gondwana Research* **18**, 230–52.

FAN, W. M., ZHANG, H. F., BAKER, J., JARVIS, K. E., MASON, P. R. D. & MENZIES, M. A. 2000. On and off the North China Craton: where is the Archean keel? *Journal of Petrology* **41**, 933–50.

FOLEY, S. F., JACKSON, S. E., FRYER, B. J., GREENOUCH, J. D. & JENNER, G. A. 1996. Trace element partition coefficients for clinopyroxene and phlogopite in an alkaline lamprophyre from Newfoundland by LAM–ICP–MS. *Geochimica et Cosmochimica Acta* **60**, 629–38.

FURNES, H., DE WIT, M. & DILEK, Y. 2014. Four billion years of ophiolites reveal secular trends in oceanic crust formation. *Geoscience Frontiers* **5**, 571–603.

GAO, S., RUDNICK, R. L., YUAN, H. L., LIU, X. M., LIU, Y. S., XU, W. L., LING, W. L., AYERS, J., WANG, X. C. & WANG, Q. H. 2004. Recycling lower continental crust in the North China Craton. *Nature* **432**, 892–97.

GAO, S., RUDNICK, R. L., XU, W. L., YUAN, H. L., LIU, Y. S., WALKER, R. J., PUCHTEL, I. S., LIU, X., HUANG, H., WANG, X. R. & YANG, J. 2008. Recycling deep cratonic lithosphere and generation of intraplate magmatism in the North China Craton. *Earth and Planetary Science Letters* **270**, 41–53.

GAO, X. Y., ZHAO, T. P. & CHEN, W. T. 2014. Petrogenesis of the early Cretaceous Funiushan granites on the southern margin of the North China Craton: implications for the Mesozoic geological evolution. *Journal of Asian Earth Sciences* **94**, 28–44.

GASPARIK, T. & LITVIN, Y. A. 2002. Experimental investigation of the effect of metasomatism by carbonatic melt on the composition and structure of the deep mantle. *Lithos* **60**, 129–43.

GIBSON, S. A. 2002. Major element heterogeneity in Archean to recent mantle plume starting-heads. *Earth and Planetary Science Letters* **195**, 59–74.

GIBSON, S. A., THOMPSON, R. N. & DICKIN, A. P. 2000. Ferropicrites: geochemical evidence for Fe-rich streaks in upwelling mantle plumes. *Earth and Planetary Science Letters* **174**, 355–74.

GREEN, N. L. 2006. Influence of slab thermal structure on basalt source regions and melting conditions: REE and HFSE constraints from the Garibaldi volcanic belt, northern Cascadia subduction system. *Lithos* **87**, 23–49.

GRIFFIN, W. L., PEARSON, N. J., BELOUSOVA, E., JACKSON, S. E., VAN ACHTERBERGH, E., O'REILLY, S. Y. & SHEE, S. R. 2000. The Hf isotope composition of cratonic mantle: LA–MC–ICP–MS analysis of zircon megacrysts in kimberlites. *Geochimica et Cosmochimica Acta* **64**, 133–47.

GROVE, T. L. & BAKER, M. B. 1984. Phase equilibrium controls on the tholeiitic versus calc-alkaline differentiation trends. *Journal of Geophysical Research* **89**, 3253–74.

HAMMOUDA, T. 2003. High-pressure melting of carbonated eclogite and experimental constraints on carbon recycling and storage in the mantle. *Earth and Planetary Science Letters* **214**, 357–68.

HART, S. R. & DUNN, T. 1993. Experimental Cpx/melt partitioning of 24 trace elements. *Contributions to Mineralogy and Petrology* **113**, 1–8.

HART, S. R., HAURI, E. H., OSCHMANN, L. A. & WHITEHEAD, J. A. 1992. Mantle plumes and entrainment: isotopic evidence. *Science* **256**, 517–9.

HAURI, E. H., WAGNER, T. P. & GROVE, T. L. 1994. Experimental and natural partitioning of Th, U, Pb and other trace elements between garnet, clinopyroxene and basaltic melts. *Chemical Geology* **117**, 149–66.

HELMY, H. M., Abd El-Rahman, Y., M., YOSHIKAWA, M., SHIBATA, T., ARAI, S., TAMURA, A. & KAGAMI, H. 2014. Petrology and Sm–Nd dating of the Genina Gharbia Alaskan-type complex (Egypt): insights into deep levels of Neoproterozoic island arcs. *Lithos* **198–199**, 263–80.

HELMY, H. M. & El Mahallawi, M., M. 2003. Gabbro Akarem mafic–ultramafic complex, Eastern Desert, Egypt: a Late Precambrian analogue of Alaskan-type complexes. *Mineralogy and Petrology* **77**, 85–108.

HELMY, H. M., YOSHIKAWA, M., SHIBATA, T., ARAI, S. & KAGAMI, H. 2015. Sm–Nd dating and petrology of Abu Hamamid intrusion, Eastern Desert, Egypt: a case of Neoproterozoic Alaskan-type complex in a backarc setting. *Precambrian Research* **258**, 234–46.

HERZBERG, C. 2006. Petrology and thermal structure of the Hawaiian plume from Mauna Kea volcano. *Nature* **444**, 605–9.

HIROSE, K. & KUSHIRO, I. 1993. Partial melting of dry peridotites at high pressures: determination of compositions of melts segregated from peridotite using aggregates of diamond. *Earth and Planetary Science Letters* **114**, 477–89.

HIRSCHMANN, M. M., KOGISO, T., BAKER, M. B. & STOLPER, E. M. 2003. Alkalic magmas generated by partial melting of garnet pyroxenite. *Geology* **31**, 481–4.

HOFMANN, A. W. 1988. Chemical differentiation of the earth: the relationship between mantle, continental crust and oceanic crust. *Earth and Planetary Science Letters* **90**, 297–314.

HOFMANN, A. W. 1997. Mantle geochemistry: the message from oceanic volcanism. *Nature* **385**, 219–29.

HOFMANN, A. W., JOCHUM, K. P., SEUFERT, M. & WHITE, W. M. 1986. Nb and Pb in oceanic basalts: new constraints on mantle evolution. *Earth and Planetary Science Letters* **79**, 33–45.

HOWARTH, G. H. & PREVEC, S. A. 2013. Hydration vs. oxidation: modelling implications for Fe–Ti oxide crystallisation in mafic intrusions, with specific reference to the Panzhihua intrusion, SW China. *Geoscience Frontiers* **4**, 555–69.

HUANG, X. L., ZHONG, J. W. & XU, Y. G. 2012. Two tales of the continental lithospheric mantle prior to the destruction of the North China Craton: insights from Early Cretaceous mafic intrusions in western Shandong, East China. *Geochimica et Cosmochimica Acta* **96**, 193–214.

ICHIYAMA, Y. & ISHIWATARI, A. 2005. HFSE-rich picritic rocks from the Mino accretionary complex, southwestern Japan. *Contributions to Mineralogy and Petrology* **149**, 373–87.

ICHIYAMA, Y., ISHIWATARI, A., HIRAHARA, Y. & SHUTO, K. 2006. Geochemical and isotopic constraints on the genesis of the Permian ferropicritic rocks from the Mino-Tamba belt, SW Japan. *Lithos* **89**, 47–65.

IRVINE, T. N. 1974. Petrology of the Duke Island ultramafic complex southeastern Alaska. *Geological Society of America Memoirs* **138**, 1–244.

IRVINE, T. N. 1979. Rocks whose composition is determined by crystal accumulation and sorting. In *The Evolution of the Igneous Rocks: Fiftieth Anniversary Perspectives* (ed. H. Yoder), pp. 245–306. Princeton: Princeton University Press.

ISHII, S., TSUNOGAE, T. & SANTOSH, M. 2006. Ultrahightemperature metamorphism in the Achankovil Zone: implications for the correlation of crustal blocks in southern India. *Gondwana Research* **10**, 99–114.

JIANG, C., JIA, C., LI, L., ZHANG, P., LU, D. & BAI, K. 2004. Source of the Fe-riched-type high-Mg magma in Mazhartag region, Xinjiang. *Acta Geologica Sinica* **78**, 770–80 (in Chinese with English abstract).

JOURDAN, F., BERTRAND, H., SCHÄRER, U., BLICHERT-TOFT, J., FËRAUD, G. & KAMPUNZU, A. B. 2007. Major and trace elements and Sr, Nd, Hf, and Pb isotope compositions of the Karoo Large Igneous Province, Botswana-Zimbabwe: lithosphere vs mantle plume contribution. *Journal of Petrology* **48**, 1043–77.

JOWITT, S. M. & ERNST, R. E. 2013. Geochemical assessment of the metallogenic potential of Proterozoic LIPs of Canada. *Lithos* **174**, 291–307.

KERRICH, R., POLAT, A., WYMAN, D. & HOLLINGS, P. 1999. Trace element systematics of Mg-, to Fe-tholeiitic basalt suites of the Superior Province: implications for Archean mantle reservoirs and greenstone belt genesis. *Lithos* **46**, 163–87.

KERRICH, R., POLAT, A. & XIE, Q. L. 2008. Geochemical systematics of 2.7 Ga Kinojevis Group (Abitibi), and Manitouwadge and Winston Lake (Wawa) Fe-rich basalt-rhyolite associations: backarc rift oceanic crust? *Lithos* **101**, 1–23.

KING, S. D. 2005. Archean cratons and mantle dynamics. *Earth and Planetary Science Letters* **234**, 1–14.

KINNAIRD, J. A., KRUGER, F. J., NEX, P. A. M. & CAWTHORN, R. G. 2002. Chromitite formation–a key to understanding processes of platinum enrichment. *Applied Earth Science, Transactions of the Institutions of Mining and Metallurgy: Section B* **111**, 23–35.

KLEMME, S., BLUNDY, J. D. & WOOD, B. J. 2002. Experimental constraints on major and trace element partitioning during partial melting of eclogite. *Geochimica et Cosmochimica Acta* **66**, 3109–23.

KOGARKO, L. N., KURAT, G. & NTAFLOS, T. 2001. Carbonate metasomatism of the oceanic mantle beneath Fernando

de Noronha Island, Brazil. *Contributions to Mineralogy and Petrology* **140**, 577–87.

Kogiso, T., Hirschmann, M. M. & Frost, D. J. 2003. High pressure partial melting of garnet pyroxenite: possible mafic lithologies in the source of ocean island basalts. *Earth and Planetary Science Letters* **216**, 603–17.

La Flèche, M. R., Camire, G. & Jenner, G. A. 1998. Geochemistry of post-Acadian, Carboniferous continental intraplate basalts from the Maritimes basin, Magdalen islands, Quebec, Canada. *Chemical Geology* **148**, 115–36.

Lassiter, J. C. & DePaolo, D. J. 1997. Plume/lithosphere interaction in the generation of continental and oceanic flood basalts: chemical and isotopic constraints. In *Large Igneous Provinces, Continental, Oceanic and Planetary Flood Volcanism* (eds. J.J. Mahoney, & M.F. Coffin), pp. 335–55. American Geophysical Union, Geophysical Monograph vol. 100. Washington, DC, USA.

Le Roex, A. P., Class, C., O'Connor, J. & Jokat, W. 2010. Shona and discovery Aseismic Ridge Systems, South Atlantic: trace element evidence for enriched mantle sources. *Journal of Petrology* **51**, 2089–120.

Leybourne, M. I., Van Wagoner, N. & Ayres, L. D. 1999. Partial melting of a refractory subducted slab in a Paleoproterozoic island arc: implications for global chemical cycles. *Geology* **27**, 731–4.

Li, N. B., Niu, H. C., Bao, Z. W., Shan, Q., Yang, W. B., Jiang, Y. H. & Zeng, L. J. 2014a. Geochronology and geochemistry of the Paleoproterozoic Fe-rich mafic sills from the Zhongtiao Mountains: petrogenesis and tectonic implications. *Precambrian Research* **255**, 668–84.

Li, S. R. & Santosh, M. 2014. Metallogeny and craton destruction: records from the North China Craton. *Ore Geology Reviews* **56**, 376–414.

Li, S. S., Santosh, M., Cen, K., Teng, X. M. & He, X. F. 2016. Neoarchean convergent margin tectonics associated with microblock amalgamation in the North China Craton: evidence from the Yishui Complex. *Gondwana Research* **38**, 113–31.

Li, S. R., Santosh, M., Zhang, H. F., Luo, J. Y., Zhang, J. Q., Li, C. L., Song, J. Y. & Zhang, X. B. 2014b. Metallogeny in response to lithospheric thinning and craton destruction: geochemistry and U–Pb zircon chronology of the Yixingzhai gold deposit, central North China Craton. *Ore Geology Reviews* **56**, 457–71.

Li, S. R., Santosh, M., Zhang, H. F., Shen, J. F., Dong, G. C., Wang, J. Z. & Zhang, J. Q. 2013. Inhomogeneous lithospheric thinning in the central North China Craton: zircon U–Pb and S–He–Ar isotopic record from magmatism and metallogeny in the Taihang Mountains. *Gondwana Research* **23**, 141–60.

Li, S., Zhao, G., Dai, L., Liu, X., Zhou, L., Santosh, M. & Su, Y. 2012. Mesozoic basins in eastern China and their bearings on the deconstruction of the North China Craton. *Journal of Asian Earth Sciences* **47**, 64–79.

Ling, W. L., Duan, R. C., Xie, X. J., Zhang, Y. Q., Zhang, J. B., Cheng, J. P., Liu, X. M. & Yang, H. M. 2009. Contrasting geochemistry of the Cretaceous volcanic suites in Shandong province and its implications for the Mesozoic lower crust delamination in the eastern North China Craton. *Lithos* **113**, 640–58.

Liu, S. W., Lü, Y. J., Wang, W., Yang, P. T., Bai, X. & Feng, Y. G. 2011. Petrogenesis of the Neoarchean granitoid gneisses in northern Hebei Province. *Acta Petrologica Sinica* **27**, 909–21 (in Chinese with English abstract).

Liu, D., Zhao, Z., Zhu, D. C., Niu, Y., DePaolo, D. J., Harrison, T. M., Mo, X., Dong, G., Zhou, S., Sun, C., Zhang, Z. & Liu, J. 2014. Postcollisional potassic and ultrapotassic rocks in southern Tibet: mantle and crustal origins in response to India–Asia collision and convergence. *Geochimica et Cosmochimica Acta* **143**, 207–31.

Liu, P. P., Zhou, M. F., Yan, D. P., Zhao, G. C., Su, S. G. & Wang, X. L. 2015. The Shangzhuang Fe-Ti oxide-bearing layered mafic intrusion, northeast of Beijing (North China): implications for the mantle source of the giant Late Mesozoic magmatic event in the North China Craton. *Lithos* **231**, 1–15.

McDonough, W. F. 1990. Constraints on the composition of the continental lithospheric mantle. *Earth and Planetary Science Letters* **101**, 1–18.

McDonough, W. F. & Sun, S. S. 1995. The composition of the Earth. *Chemical Geology* **120**, 223–54.

McKenzie, D. & O'Nions, R. K. 1991. Partial melt distribution from inversion of rare earth element concentrations. *Journal of Petrology* **32**, 1021–91.

Menzies, M. A., Fan, W. M. & Zhang, M. 1993. Palaeozoic and Cenozoic lithoprobes and loss of >120 km of Archean lithosphere, Sino-Korean craton, China. In *Magmatic Processes and Plate Tectonics* (eds H. M. Prichard, T. Alabaster, N. B. W. Harris & C. R. Neary), pp. 71–81. Geological Society of London, Special Publication no. 76.

Menzies, M. A., Xu, Y. G., Zhang, H. F. & Fan, W. M. 2007. Integration of geology, geophysics and geochemistry: a key to understanding the North China Craton. *Lithos* **96**, 1–21.

Morse, S. A. 1968. Layered intrusions and anorthosite genesis. In *Origin of Anorthosite and Related Rocks* (ed. Y. W. Isachsen), pp. 175–87. New York State Museum and Science Memoir 18.

Naldrett, A. J. & von Gruenewaldt, G. 1989. Association of platinum-group elements with chromitite in layered intrusions and ophiolite complexes. *Economic Geology* **84**, 180–87.

Neumann, E. R., Svensen, H., Galerne, C. Y. & Plamke, S. 2011. Multistage evolution of dolerites in the Karoo Large Igneous Province, Central South Africa. *Journal of Petrology* **52**, 952–84.

Nyblade, A. A. 2001. Earth science: hard-cored continents. *Nature* **411**, 38–9.

Pearce, J. A. 2008. Geochemical fingerprinting of oceanic basalts with applications to ophiolite classification and the search for Archean oceanic crust. *Lithos* **100**, 14–48.

Pearce, J. A. & Stern, R. J. 2006. Origin of back-arc basin margins: trace element and isotope perspectives. In *Back-Arc Spreading Systems: Geological, Biological, Chemical, and Physical Interactions* (D. M. Christie, C. R. Fisher, S.-M. Lee & S. Givens), pp. 63–86. American Geophysical Union, Geophysical Monograph vol. **166**. Washington, DC, USA.

Peate, D. W. 1997. The Paraná-Etendeka Province. In *Large Igneous Provinces* (eds J. J. Mahoney & M. F. Coffin), pp. 217–45. American Geophysical Union, Geophysical Monograph vol. **100**. Washington, DC, USA.

Polat, A., Appel, P. W. U. & Fryer, B. J. 2011. An overview of the geochemistry of Eoarchean to Mesoarchean ultramafic to mafic volcanic rocks, SW greenland: implications for mantle depletion and petrogenetic processes at subduction zones in the early Earth. *Gondwana Research* **20**, 255–83.

POLAT, A. & HOFMANN, A. W. 2003. Alteration and geochemical patterns in the 3.7–3.8 Ga Isua greenstone belt, West Greenland. *Precambrian Research* **126**, 197–218.

REUBI, O., SIMS, K. W. W. & BOURDAN, B. 2014. ^{238}U–^{230}Th equilibrium in arc magmas and implications for the time scales of mantle metasomatism. *Earth and Planetary Science Letters* **391**, 146–58.

ROEDER, P. L. & EMSLIE, R. F. 1970. Olivine–liquid equilibrium. *Contributions to Mineralogy and Petrology* **29**, 275–89.

RUDNICK, R. L. 2005. Destruction of cratonic lithosphere: the North China Craton. In *AGU Fall Meeting. AGU Fall Meeting Abstract #T22B-05*.

RUDNICK, R. L. & GAO, S. 2003. Composition of the continental crust. In *The Crust* Pergamon (ed. R. L. Rudnick), pp. 1–64. Oxford: Elsevier.

RUDNICK, R. L., GAO, S., LING, W. L., LIU, Y. S. & MCDONOUGH, W. F. 2004. Petrology and geochemistry of spinel peridotite xenoliths from Hannuoba and Qixia, North China Craton. *Lithos* **77**, 609–37.

SANTOSH, M. 2010. Assembling North China Craton within the Columbia supercontinent: the role of double-sided subduction. *Precambrian Research* **178**, 149–67.

SANTOSH, M., TENG, X. M., HE, X. F., TANG, L. & YANG, Q. Y. 2016. Discovery of Neoarchean suprasubduction zone ophiolite suite from Yishui Complex in the North China Craton. *Gondwana Research* **38**, 1–27.

SANTOSH, M., YANG, Q. Y., TENG, X. M. & TANG, L. 2015. Paleoproterozoic crustal growth in the North China Craton: evidence from the Lüliang Complex. *Precambrian Research* **263**, 197–231.

SAUNDERS, A. D., STOREY, M., KENT, R. W. & NORRY, M. J. 1992. Consequences of plume–lithosphere interactions. In *Magmatism and the Causes of Continental Break-up* (eds T. Alabaster, B.C. Storey & R.J. Pankhurst), pp. 41–60. Geological Society of London, Special Publication no. 68.

SEO, J., OH, C. W., CHOI, S. G. & RAJESH, V. J. 2013. Two ultramafic rock types in the Hongseong area, South Korea: tectonic significance for northeast Asia. *Lithos* **175–176**, 30–9.

SHAPIRO, S. S., HAGER, B. H. & JORDAN, T. H. 1999. Stability and dynamics of the continental tectosphere. *Lithos* **48**, 115–33.

SISSON, T. W., GROVE, T. L. & COLEMAN, D. S. 1996. Hornblende gabbro sill complex at Onion Valley, California, and a mixing origin for the Sierra Nevada batholith. *Contributions to Mineralogy and Petrology* **126**, 81–108.

SKOVGAARD, A. C., STOREY, M., BAKER, J., BLUSZTAJN, J. & HART, S. R. 2001. Osmium–oxygen isotopic evidence for a recycled and strongly depleted component in the Iceland mantle plume. *Earth and Planetary Science Letters* **194**, 259–75.

SLAGSTAD, T., JAMIESON, R. A. & CULSHAW, N. G. 2005. Formation, crystallization, and migration of melt in the midorogenic crust: Muskoka Domain migmatites, Grenville Province, Ontario. *Journal of Petrology* **46**, 893–919.

SMITH, T. E., HUANG, C. H., WALAWENDER, M. J., CHEUNG, P. & WHEELER, C. 1983. The gabbroic rocks of the Peninsular Ranges batholith, southern California: cumulate rocks associated with calc-alkalic basalts and andesites. *Journal of Volcanology and Geothermal Research* **18**, 249–78.

SOBOLEV, A. V., HOFMANN, A. W., SOBOLEV, S. V. & NIKOGOSIAN, I. K. 2005. An olivine-free mantle source of Hawaiian shield basalts. *Nature* **434**, 590–97.

SÖDERLUND, U., PATCHETT, P. J., VERVOORT, J. D. & ISACHSEN, C. E. 2004. The ^{176}Lu decay constant determined by Lu–Hf and U–Pb isotope systematics of Precambrian mafic intrusions. *Earth and Planetary Science Letters* **219**, 311–24.

SPANDLER, C., YAXLEY, G., GREEN, D. H. & ROSENTHAL, A. 2008. Phase relations and melting of anhydrous K-bearing eclogite from 1200 to 1600 °C and 3 to 5 GPa. *Journal of Petrology* **49**, 771–95.

SU, S. G., DENG, J. F., ZHAO, G. C., ZHAO, X. G. & LIU, C. 2006. Characteristics, origin and resource property of Xuejiashiliang Complex, Beijing area and their relationship with the way of lithospheric thinning. *Earth Science Frontiers* **13**, 148–57.

SU, S. G., NIU, Y. L., DENG, J. F., LIU, C., ZHAO, G. C. & ZHAO, X. G. 2007. Petrology and geochronology of Xuejiashiliang igneous complex and their genetic link to the lithospheric thinning during the Yanshanian orogenesis in eastern China. *Lithos* **96**, 90–107.

SU, B. X., QIN, K. Z., SUN, H., TANG, D. M., SAKYI, P. A., CHU, Z. Y., LIU, P. P. & XIAO, Q. H. 2012. Subduction-induced mantle heterogeneity beneath Eastern Tianshan and Beishan: insights from Nd–Sr–Hf–O isotopic mapping of Late Paleozoic mafic–ultramafic complexes. *Lithos* **134–135**, 41–51.

SUN, S. S. & MCDONOUGH, W. F. 1989. Chemical and isotopic systematics of oceanic basalts: implications for mantle composition and process. In *Magmatism in the Ocean Basin* (A. D. Saunders & M. J. Nony), pp. 313–54. Geological Society of London, Special Publication no. 42.

TANG, L., SANTOSH, M., TSUNOGAE, T. & TENG, X. M. 2016. Late Neoarchean arc magmatism and crustal growth associated with microblock amalgamation in the North China Craton: evidence from the Fuping complex. *Lithos* **248**, 324–38.

TEMIZEL, I., ARSLAN, M., RUFFET, G. & PEUCAT, J. J. 2012. Petrochemistry, geochronology and Sr–Nd isotopic systematics of the Tertiary collisional and post-collisional volcanic rocks from the Ulubey (Ordu) area, eastern Pontide, NE Turkey: implications for extension-related origin and mantle source characteristics. *Lithos* **128**, 126–47.

TENG, X. M. & SANTOSH, M. 2015. A long-lived magma chamber in the Paleoproterozoic North China Craton: evidence from the Damiao gabbro–anorthosite suite. *Precambrian Research* **256**, 79–101.

TENG, X. M., SANTOSH, M., TSUNOGAE, T. & TANG, L. 2016. Magma chamber processes in Early Cretaceous Shangzhuang layered mafic intrusion from the North China Craton. *Geological Journal*, published online 30 August 2016. doi: 10.1002/gj.2856.

TENG, X. M., YANG, Q. Y. & SANTOSH, M. 2015. Devonian magmatism associated with arc-continent collision in the northern North China Craton: evidence from the Longwangmiao ultramafic intrusion in the Damiao area. *Journal of Asian Earth Sciences* **113**, 626–43.

TIAN, W., CHEN, B., LIU, C. Q. & ZHANG, H. F. 2007. Zircon U–Pb age and Hf isotopic composition of the Xiaozhangjiakou ultramafic pluton in northern Hebei. *Acta Petrologica Sinica* **23**, 583–90 (in Chinese with English abstract).

TOLLARI, N., BARNES, S. J., COX, R. A. & NABIL, H. 2008. Trace element concentrations in apatites from the

Sept-Iles intrusion suite, Canada – implications for the genesis of nelsonites. *Chemical Geology* **252**, 180–90.

VAN DE ZEDDE, D. M. A. & WORTEL, M. J. R. 2001. Shallow slab detachment as a transient source of heat at mid lithospheric depths. *Tectonics* **20**, 868–82.

VERVOORT, J. D. & PATCHETT, P. J. 1996. Behavior of hafnium and neodymium isotopes in the crust: constraints from Precambrian crustally derived granites. *Geochimica et Cosmochimica Acta* **60**, 3717–33.

VON GRUENEWALDT, G. & HARMER, R. E. 1992. Chapter 5: Tectonic setting of Proterozoic layered intrusions with special reference to the Bushveld complex. In *Developments in Precambrian Geology* (ed K. C. Condie), pp. 181–213. Amsterdam: Elsevier.

WAGER, L. R. & BROWN, G. M. 1968. *Layered Igneous Rock*. Edinburgh: Oliver & Boyd, 588 pp.

WALLACE, M. L., JOWITT, S. M. & SALEEM, A. 2015. Geochemistry and petrogenesis of mafic-ultramafic suites of the Irindina Province, Northern Territory, Australia: implications for the Neoproterozoic to Devonian evolution of central Australia. *Lithos* **234–235**, 61–78.

WANG, Y. J., FAN, W. M., ZHANG, Y. H., GUO, F., ZHANG, H. F. & PENG, T. P. 2004. Geochemical, ^{40}Ar/^{39}Ar geochronological and Sr–Nd isotopic constraints on the origin of Paleoproterozoic mafic dikes from the southern Taihang Mountains and implications for the ca. 1800 Ma event of the North China Craton. *Precambrian Research* **135**, 55–77.

WANG, T., GUO, L., ZHENG, Y., DONSKAYA, T., GLADKOCHUB, D., ZENG, L., LI, J., WANG, Y. & MAZUKABZOV, A. 2012. Timing and processes of late Mesozoic mid-lower-crustal extension in continental NE Asia and implications for the tectonic setting of the destruction of the North China Craton: mainly constrained by zircon U–Pb ages from metamorphic core complexes. *Lithos* **154**, 315–45.

WANG, Y. & ZHANG, Q. 2001. A granitoid complex from Badaling area, North China: composition, geochemical characteristics and its implications. *Acta Petrologica Sinica* **17**, 533–40 (in Chinese with English abstract).

WILSON, B. M. 1989. *Igneous Petrogenesis: A Global Tectonic Approach*. Berlin: Springer.

WILSON, M. 2001. *Igneous Petrogenesis*. London: Unwin Hyman.

WINCHESTER, J. A. & FLOYD, P. A. 1976. Geochemical magma type discrimination: application to altered and metamorphosed basic igneous rocks. *Earth and Planetary Science Letters* **28**, 459–69.

WINDLEY, B. F., ALEXEIEV, D., XIAO, W., KRÖNER, A. & BADARCH, G. 2007. Tectonic models for accretion of the Central Asian Orogenic Belt. *Journal of the Geological Society, London* **164**, 31–47.

WORKMAN, R. K., HART, S. R., BLUSZTAJN, J., JACKSON, M., KURZ, M. & STAUDIGEL, H. 2003. Enriched mantle II: a new view from the Samoan hotspot. *Geophysical Research Abstract* **5**, 13656.

WU, F. Y., LI, X. H., ZHENG, Y. F. & GAO, S. 2007. Lu–Hf isotopic systematics and their applications in petrology. *Acta Petrologia Sinica* **23**, 185–220 (in Chinese with English abstract).

WU, F. Y., LIN, J. Q., WILDE, S. A., ZHANG, X. O. & YANG, J. H. 2005. Nature and significance of the Early Cretaceous giant igneous event in eastern China. *Earth and Planetary Science Letters* **233**, 103–19.

XIAO, W., WINDLEY, B. F., HAO, J. & ZHAI, M. G. 2003. Accretion leading to collision and the Permian Solonker suture, Inner Mongolia, China: termination of

the central Asian orogenic belt. *Tectonics* **22**, 1069. doi: 10.1029/2002TC001484.

XIAO, Y., ZHANG, H. F., FAN, W. M., YING, J. F., ZHANG, J., ZHAO, X. M. & SU, B. X. 2010. Evolution of lithospheric mantle beneath the Tan–Lu fault zone, eastern North China Craton: evidence from petrology and geochemistry of peridotite xenoliths. *Lithos* **117**, 229–46.

XIE, Q., ZHANG, Z., HOU, T., SANTOSH, M., JIN, Z., HAN, L. & CHENG, Z. 2015. Petrogenesis of the Zhangmatun gabbro in the Ji'nan complex, North China Craton: implications for skarn-type iron mineralization. *Journal of Asian Earth Sciences* **113**, 1197–217.

XU, Y. G., HUANG, X. L., MA, J. L., WANG, Y. B., LIZUKA, Y., XU, J. F., WANG, Q. & WU, X. Y. 2004*a*. Crust–mantle interaction during the tectono-thermal reactivation of the North China Craton: constraints from SHRIMP zircon U–Pb chronology and geochemistry of Mesozoic plutons from western Shandong. *Contributions to Mineralogy and Petrology* **147**, 750–67.

XU, Y. G., MA, J. L., HUANG, X. L., LIZUKA, Y., CHUNG, S. L., WANG, Y. B. & WU, X. Y. 2004*b*. Early Cretaceous gabbroic complex from Yinan, Shandong Province: petrogenesis and mantle domains beneath the North China Craton. *International Journal of Earth Sciences* **93**, 1025–41.

XU, Y. G., MEI, H. J., XU, J. F., HUANG, X. L., WANG, Y. J. & CHUNG, S. L. 2003. Origin of two differentiation trends in the Emeishan flood basalts. *Chinese Science Bulletin* **48**, 390–94.

YANG, Q. Y. & SANTOSH, M. 2015. Early Cretaceous magma flare-up and its implications on gold mineralization in the Jiaodong Peninsula, China. *Ore Geology Reviews* **65**, 626–42.

YANG, Q. Y. & SANTOSH, M. 2017. The building of an Archean microcontinent: Evidence from the North China Craton. *Gondwana Research*, published online 24 January 2017. doi: 10.1016/j.gr.2017.01.003.

YANG, Q. Y., SANTOSH, M., COLLINS, A. S. & TENG, X. M. 2016. Microblock amalgamation in the North China Craton: evidence from Neoarchaean magmatic suite in the western margin of the Jiaoliao Block. *Gondwana Research* **31**, 96–123.

YANG, Q. Y., SANTOSH, M., SHEN, J. F. & LI, S. R. 2014. Juvenile vs. recycled crust in NE china: zircon U–Pb geochronology, Hf isotope and an integrated model for Mesozoic gold mineralization in the Jiaodong Peninsula. *Gondwana Research* **25**, 1445–68.

YANG, J. H., WU, F. Y., CHUNG, S. L., LO, C. H., WILDE, S. A. & DAVIS, G. A. 2007. Rapid exhumation and cooling of the Liaonan metamorphic core complex: inferences from ^{40}Ar/^{39}Ar thermochronology and implications for Late Mesozoic extension in the eastern North China Craton. *Geological Society of America Bulletin* **119**, 1405–14.

YANG, J. H., WU, F. Y., CHUNG, S. L., WILDE, S. A. & CHU, M. F. 2006a. A hybrid origin for the Qianshan A-type granite, northeast China: geochemical and Sr–Nd–Hf isotopic evidence. *Lithos* **89**, 89–106.

YANG, J. H., WU, F. Y., CHUNG, S. L., WILDE, S. A., CHU, M. F., LO, C. H. & SONG, B. 2005. Petrogenesis of Early Cretaceous intrusions in the Sulu ultrahigh-pressure orogenic belt, east China and their relationship to lithospheric thinning. *Chemical Geology* **222**, 200–31.

YANG, J. H., WU, F. Y., SHAO, J. A., XIE, L. W. & LIU, X. M. 2006b. In-situ U–Pb dating and Hf isotopic analyses of zircons from volcanic rocks of the Houcheng and Zhangjiakou Formations in the Zhuang–Xuan area, northeast China. *Earth Science–Journal of China*

University of Geosciences **31**, 71–80 (in Chinese with English abstract).

YANG, D. B., XU, W. L., PEI, F. P., YANG, C. H. & WANG, Q. H. 2012. Spatial extent of the influence of the deeply subducted South China Block on the southeastern North China Block: constraints from Sr–Nd–Pb isotopes in Mesozoic mafic igneous rocks. *Lithos* **136**, 246–60.

YING, J. F., ZHANG, H. F., KITA, N., MORISHITA, Y. & SHIMODA, G. 2006. Nature and evolution of Late Cretaceous lithospheric mantle beneath the eastern North China Craton: constraints from petrology and geochemistry of peridotitic xenoliths from Junan, Shandong Province, China. *Earth and Planetary Science Letters* **244**, 622–38

YUAN, H. L., GAO, S., LIU, X. M., LI, H. M., GUNTHER, D. & WU, F. Y. 2004. Accurate U–Pb age and trace element determination of zircon by laser ablation-inductively coupled plasma-mass spectrometry. *Geostandards and Geoanalytical Research* **28**, 353–70.

ZHAI, M. G. & SANTOSH, M. 2011. The early Precambrian odyssey of the North China Craton: a synoptic overview. *Gondwana Research* **20**, 6–25.

ZHANG, H. F., SUN, M., ZHOU, M. F., FAN, W. M., ZHOU, X. H. & ZHAI, M. G. 2004. Highly heterogeneous Late Mesozoic lithospheric mantle beneath the North China Craton: evidence from Sr–Nd–Pb isotopic systematics of mafic igneous rocks. *Geological Magazine* **141**, 55–62.

ZHANG, H. F., SUN, M., ZHOU, X. H., ZHOU, M. F., FAN, W. M. & ZHENG, J. P. 2003. Secular evolution of the lithosphere beneath the eastern North China Craton: evidence from Mesozoic basalts and high-Mg andesites. *Geochimica et Cosmochimica Acta* **67**, 4373–87.

ZHANG, H. F. & YANG, Y. H. 2007. Emplacement age and Sr–Nd–Hf isotopic characteristics of the diamondiferous kimberlites from the eastern North China Craton. *Acta Petrologica Sinica* **23**, 285–94 (in Chinese with English abstract).

ZHANG, S. H., ZHAO, Y., DAVIS, G. A., YE, H. & WU, F. 2014. Temporal and spatial variations of Mesozoic magmatism and deformation in the North China Craton: im-plications for lithospheric thinning and decratonization. *Earth-Science Reviews* **131**, 49–87.

ZHANG, S. H., ZHAO, Y., KRÖNER, A., LIU, X. M., XIE, L. W. & CHEN, F. K. 2009a. Early Permian plutons from the northern North China Block: constraints on continental arc evolution and convergent margin magmatism related to the Central Asian Orogenic Belt. *International Journal of Earth Sciences* **98**, 1441–67.

ZHANG, S. H., ZHAO, Y., LIU, X. C., LIU, D. Y., CHEN, F., XIE, L. W. & CHEN, H. H. 2009b. Late Paleozoic to Early Mesozoic mafic–ultramafic complexes from the northern North China Block: constraints on the composition and evolution of the lithospheric mantle. *Lithos* **110**, 229–46.

ZHANG, S. H., ZHAO, Y., SONG, B. & LIU, D. Y. 2007. Petrogenesis of the Middle Devonian Gushan diorite pluton on the northern margin of the North China block and its tectonic implications. *Geological Magazine* **144**, 553–68.

ZHAO, G. C., SUN, M., WILDE, S. A. & LI, S. Z. 2005. Late Archean to Paleoproterozoic evolution of the North China Craton: key issues revisited. *Precambrian Research* **136**, 177–202.

ZHAO, G. C. & ZHAI, M. G. 2013. Lithotectonic elements of Precambrian basement in the North China Craton: review and tectonic implications. *Gondwana Research* **23**, 1207–40.

ZHENG, J. P., O'REILLY, S. Y., GRIFFIN, W. L., LU, F. X., ZHANG, M. & PEARSON, N. J. 2001. Relict refractory mantle beneath the eastern North China block: significance for lithosphere evolution. *Lithos* **57**, 43–66.

ZHENG, J. P., SUN, M., ZHOU, M. F. & ROBINSON, P. 2005. Trace elemental and PGE geochemical constraints of Mesozoic and Cenozoic peridotitic xenoliths on lithospheric evolution of the North China Craton. *Geochimica et Cosmochimica Acta* **69**, 3401–18.

ZHU, Y., GUO, X., SONG, B., ZHANG, L. & GU, L. 2009. Petrology, Sr–Nd–Hf isotopic geochemistry and zircon chronology of the Late Paleozoic volcanic rocks in the southwestern Tianshan Mountains, Xinjiang, NW China. *Journal of Geological Society, London* **166**, 1085–99.